

Université Mohamed Khider – Biskra

Faculté des Sciences et de la technologie

Département : Génie électrique

Ref :



جامعة محمد خيضر بسكرة
كلية العلوم و التكنولوجيا
قسم: هندسة كهربائية
المرجع:

Thèse présentée en vue de l'obtention
Du diplôme de
Doctorat en sciences

Spécialité : Electronique

Conception d'un transistor bipolaire à base de Si/SiGe par SILVACO

Présentée par :
Abdelkader KHADIR

Soutenue publiquement le : 30/01/2019

Devant le jury composé de :

MEFTAH Afak	Professeur	Président	Université de Biskra
SENGOUGA Nouredine	Professeur	Rapporteur	Université de Biskra
DEHIMI Lakhdar	Professeur	Examinateur	Université de Batna
GUEDDIM Ahmed	Professeur	Examinateur	Université de Djelfa

ACKNOWLEDGMENTS

First of all I would like to thank God who gives me the opportunity and ability to take this challenging task. Secondly, I would like to thank my supervisor Prof. Nouredine SENGOUGA for his patience, instructions and encouragement. I would also like to thank Professors Afak Meftah, Lakdar Dehimi and Ahmed Gueddim for accepting to examine my humble work.

Finally, I would like to express my deepest gratitude to my family to have supported me throughout this experience.

DEDICATION

For my father's and mother's souls

For my wife

For Sabrine, Farouk, Nour elhouda and Ahmed, god's awesome gifts.

ABSTRACT

This work present a numerical simulation of the effects of emitter and collector widths of a Bipolar Transistor based on a heterojunction between Silicon and Silicon-Germanium (Si/SiGe HBT) on its performance. Firstly the direct and transfer current-voltage characteristics are evaluated. Secondly the HBT figures of merit such as the direct current (DC) current gain β_F , cutoff frequency f_T , and maximum oscillation frequency f_{MAX} are calculated. The drift-diffusion (DD) and energy balance (EB) models used to calculate the above characteristics and figures of merit are then compared. The numerical simulation is achieved through the use of the different models available from SILVACO technology computer-aided design (T-CAD).

We considered seven SiGe HBTs devices depending on emitter and collector widths. The influence of emitter and collector widths on the current gain, the cutoff frequency and the maximum oscillation frequency for each device was simulated. The obtained DC current gain values using the EB model are much higher than those obtained using the DD model. The change in the current gain values for the seven devices was not significant when using either the EB or DD model. The cutoff frequency obtained using the EB model was much higher than when using the DD model. The maximum oscillation frequency values obtained using the EB model were close to those obtained using the DD. Based on the EB simulation results, reduction of the emitter width (W_E) while keeping the collector width (W_C) unchanged causes an increase in the cutoff frequency and the maximum oscillation frequency; these results show that one can improve both f_T and f_{MAX} with no remarkable change in β_F by making a tradeoff between the widths W_E and W_C without shrinking the transistor regions.

The effect of the trapezoidal profile shape of the germanium in the base and the base doping were also studied. In the case of changing the germanium profile shape, it was found that the values of the current gain using EB model are higher than the HD ones and much higher than the DD ones. The results of f_{MAX} using HD and EB transport models shows that the germanium profile shape is of great importance in the design of SiGe HBTs.

Concerning the doping effects, the simulation results using energy balance model show that the base doping affects considerably both the current gain and the frequencies where it improves f_{MAX} and decreases the current gain.

Key words: SiGe HBT, current gain, cut-off frequency, maximum oscillation frequency, SILVACO.

RESUMÉ

Ce travail présente une simulation numérique des effets des largeurs d'émetteur et du collecteur sur les performances d'un transistor bipolaire basé sur une hétérojonction entre le silicium et le silicium-germanium (Si / SiGe HBT). Premièrement, les caractéristiques de courant continu et de transfert courant-tension ont été évaluées. Deuxièmement, les facteurs de mérite HBT telles que le gain de courant β_F , la fréquence de coupure f_T et la fréquence d'oscillation maximale f_{MAX} ont été calculés. Les modèles de dérive-diffusion (DD) et d'énergie-balance (EB) ont été utilisés pour calculer les caractéristiques ci-dessus et les facteurs de mérite ont été ensuite comparés. La simulation numérique est réalisée grâce à l'utilisation des différents modèles proposés par la technologie de conception assistée par ordinateur (T-CAD) de SILVACO. Nous avons considéré sept dispositifs TBH à base de SiGe en fonction de la largeur de l'émetteur et du collecteur. L'influence de la largeur de l'émetteur et du collecteur sur le gain de courant, la fréquence de coupure et la fréquence d'oscillation maximale de chaque dispositif a été simulée. Les valeurs de gain en courant continu obtenues à l'aide du modèle EB sont beaucoup plus élevées que celles obtenues à l'aide du modèle DD. La différence entre les valeurs du gain de courant pour les sept dispositifs n'était pas significative pour chacun des modèles EB ou DD. La fréquence de coupure obtenue avec le modèle EB était beaucoup plus élevée qu'avec le modèle DD. Les valeurs de fréquence d'oscillation maximale obtenues avec le modèle EB étaient proches de celles obtenues avec le modèle DD. Sur la base des résultats de la simulation EB, la réduction de la largeur de l'émetteur W_E tout en maintenant la largeur du collecteur W_C inchangée entraîne une augmentation de la fréquence de coupure et de la fréquence d'oscillation maximale. Ces résultats montrent que l'on peut améliorer à la fois f_T et f_{MAX} sans changement notable de β_F en effectuant un compromis entre les largeurs W_E et W_C sans miniaturiser les régions du transistor. L'effet de la forme trapézoïdal du profil du germanium dans la base et du dopage de la base a été également étudié. Dans le cas de la modification de la forme du profil trapézoïdal du germanium, il a été constaté que les valeurs du gain de courant en utilisant le modèle EB sont supérieures à celles en utilisant HD et beaucoup plus supérieures à celles en utilisant DD. Les résultats de f_{MAX} avec l'utilisation des modèles de transport HD et EB montrent que la forme trapézoïdal du profile du germanium a une grande importance dans la conception des TBHs à base de SiGe. En ce qui concerne les effets du dopage, les résultats de la simulation en utilisant le modèle EB montrent que le dopage de base affecte considérablement le gain de courant et les fréquences où l'augmentation du dopage améliore f_{MAX} et cause la diminution du gain de courant.

Mots-clés: SiGe TBH, gain de courant, fréquence de coupure, fréquence d'oscillation maximale, SILVACO.

ملخص

يقدم هذا العمل محاكاة عدبية لتأثيرات عرض الباوث والجامع على أداء الترانزستور ثنائي القطب ذي بنية غير متجانسة (HBT) بأساس SiGe. أولاً يتم تقييم الخصائص المباشرة وخصائص تحويل تيار جهد. ثانياً يتم حساب كسب التيار المباشر (DC) β_F ، تردد القطع f_T و تردد التذبذب الأقصى f_{MAX} ثم تتم مقارنتها باستخدام نماذج الانجراف - الانبعاث (DD) وتوازن الطاقة (EB) من تكنولوجيا تصميم الكمبيوتر المساعد (T-CAD) SILVACO. تمت دراسة سبعة أجهزة SiGe HBTs اعتماداً على عرض كلا من الباوث والجامع . تم محاكاة تأثير عرض الباوث و الجامع على كسب التيار، تردد القطع و تردد التذبذب الأقصى لكل جهاز . لوحظ أن قيم كسب التيار المستمر التي تم الحصول عليها باستخدام نموذج EB أعلى بكثير من تلك التي تم الحصول عليها باستخدام نموذج DD. نشير إلى أن التغير في قيم كسب التيار للأجهزة السبعة لم يكن هاماً عند استخدام نموذج EB وكذلك بالنسبة للأجهزة السبعة باستخدام نموذج DD. تردد القطع الذي تم الحصول عليه باستخدام نموذج EB أعلى بكثير من استخدام نموذج DD. قيم تردد التذبذب الأقصى التي تم الحصول عليها باستخدام نموذج EB كانت قريبة من تلك التي تم الحصول عليها باستخدام نموذج DD. استناداً إلى نتائج المحاكاة باستعمال نموذج EB ، يؤدي خفض عرض المرسل (W_E) مع الحفاظ على عرض المجمع (W_C) دون تغيير إلى زيادة في تردد القطع و تردد التذبذب الأقصى. تظهر النتائج الأخيرة إلى أنه يمكن تحسين كلا من f_T و f_{MAX} دون تسجيل انخفاض ملحوظ في β_F وذلك عن طريق إجراء مقاييس بين العرضين W_E و W_C دون اللجوء إلى تقليص مساحة مناطق الترانزستور.

كما تمت دراسة تأثير تغيير شكل مظهر شبه المنحرف للجيرمانيوم في القاعدة وتأثير تعليم القاعدة على كفاءة HBTs . في حالة تغيير شكل المظهر الجانبي للجيرمانيوم ، وجد أن قيم كسب التيار باستخدام نموذج EB أعلى من قيم HD وأعلى بكثير من قيم DD . وتبين نتائج f_{MAX} التي تستخدم نماذج نقل HD و EB أن شكل المظهر الجانبي لشبه المنحرف للجيرمانيوم له أهمية كبيرة في تصميم SiGe HBTs . أما فيما يتعلق بتأثيرات تعليم القاعدة ، تظهر نتائج المحاكاة انه باستخدام نموذج EB أن تعليم القاعدة يؤثر بشكل كبير على كل من كسب التيار والترددات حيث يعمل على تحسين f_{MAX} ويقلل من كسب التيار.

الكلمات المفتاحية: ترانزستور سيليسيوم-جرمانيوم ثنائي القطبية هجين البنية، كسب التيار، تردد القطع، تردد التذبذب الأقصى، سيلفاكو.

Table of contents	
Acknowledgment	i
Dedication	ii
Abstract	iii
Résumé	iv
ملخص	v
Table of contents	vi
List of figures	x
List of tables	xii
List of acronyms	xiii
List of symbols	xiv
Introduction	1
Chapter I : Silicon bipolar and silicon-germanium hetero-junction bipolar transistors principles	
I.1 Introduction	5
I.2 Elemental semiconductors: silicon and germanium	5
I.2.1 Crystal structure	6
I.2.2 Band structure	7
I.3 PN junction	8
I.4 Bipolar junction transistor	10
I.4.1 Base current	11
I.4.2 Collector current	13
I.4.3 Current gain	14
I.5 Silicon-Germanium Heterojunction Bipolar Transistors.	14
I.5.1 Current gain	15
I.5.2 The transit time	16
I.5.3 Cut-off frequency f_T	16
I.5.4 Maximum oscillation frequency f_{MAX}	18
I.5.5 Base, collector and emitter resistance	18
I.5.5.1 Base Resistance	19
I.5.5.2 Collector Resistance	20
I.5.6 Emitter/base and collector/base depletion capacitance	21
I.6 Strain, dislocations and critical thickness	21
References	25

Chapter II: Si and SiGe Physical models	
II.1 Introduction	27
II.2 The energy balance model	27
II.3 SiGe material characteristics	30
II.3.1 Bandgap	31
II.3.2 Electron Affinity	31
II.3.3 Density of States	31
II.3.4 Dielectric Function	31
II.3.5 Low Field Mobility	31
II.3.6 Velocity Saturation	32
II.4 Si and SiGe physical models	32
II.4.1 Band-gap narrowing	32
II.4.2 Shockley-Read-Hall (SRH) Recombination	33
II.4.2.1 SRH Concentration-Dependent Lifetime Model	34
II.4.3 Field dependent mobility	35
II.4.4 Low Field Mobility Models	35
II.4.4.1 Parallel Electric Field-Dependent Mobility Models	36
II.4.4.2 Concentration-Dependent Low-Field Mobility	37
II.4.5 Statistics of Fermi-Dirac	38
II.4.6 Auger Recombination	39
II.4.6.1 Standard Auger Model	39
References	40
Chapter III: SILVACO Atlas T-CAD Device Simulator	
III.1 Introduction	43
III.2 Simulation history	43
III.3 ATLAS device simulator	43
III.3.1 Operation of ATLAS	44
III.4 ATLAS Commands organization	44
III.4.1 Structure Specification	45
III.4.1.1 Mesh	45
III.4.1.2 Region	47
III.4.1.3 Electrodes	47
III.4.1.4 Doping	47

III.4.2 Materials Model Specification	48
III.4.2.1 Specifying Material Properties	48
III.4.2.1.1 Semiconductor, Insulator, or Conductor	48
III.4.2.1.2 Setting Parameters	49
III.4.2.2 Specifying Physical Models	49
III.4.2.2.1 Using the C-Interpreter to Specify Models	49
III.4.2.3 Contact Characteristics	49
III.4.2.3.1 Workfunction for Gates or Schottky Contacts	50
III.4.2.3.2 Shorting Two Contacts Together	50
III.4.3 Numerical Methods	50
III.4.3.1 Numerical Solution Techniques	50
III.4.3.2 Basic Drift Diffusion Calculations	51
III.4.3.3 Energy Balance Calculations	51
III.4.4 Solution Specification	51
III.4.4.1 DC Solutions	51
III.4.4.1.1 Sweeping the Bias	52
III.4.4.1.2 Initial Guess Importance	52
III.4.4.1.3 The Initial Solution	52
III.4.4.1.4 The First and Second Non-Zero Bias Solutions	52
III.4.4.1.5 The Trap Parameter	53
III.4.4.2 Small-Signal AC Solutions	53
III.4.4.2.1 Ramped Frequency at a Single Bias	53
III.4.4.3 Run-Time Output	53
III.4.4.4 Log Files	55
III.5 Results analysis	56
III.5.1 Parameter Extraction in DeckBuild	56
III.5.2 Solution Files (tonyplot)	56
References	58
Chapter IV: Results And Discussions	
IV.1 Introduction	59
IV.2 Effect of emitter and intrinsic collector widths on SiGe HBT performance	59
IV.2.1 Device structure	60
IV.2.2 Effect of emitter and intrinsic collector widths on the current gain	61

IV.2.3 Effect of emitter and intrinsic collector widths on the gummel Plots	63
IV.2.4 Effect of emitter and intrinsic collector widths on the cut-off frequency and the maximum oscillation frequency	64
IV.2.5 Effect of emitter and intrinsic collector widths on the forward transit time	67
IV.3 Effect of germanium trapezoidal profile shapes on SiGe HBT Performance	68
IV.3.1 Device structure	68
IV.3.2 Effect of germanium trapezoidal profile shapes on the DC current Gain	68
IV.3.3 Effect of germanium profile shapes on the gummel plots	70
IV.3.4 Effect of germanium profile shapes on the cut-off frequency and the maximum oscillation frequency	70
IV.4 Effect of base doping on SiGe HBT performance	72
IV.4.1 Device structure	72
IV.4.2 Effect of base doping on current gain	72
IV.4.3 Effect of base doping on gummel plots	73
IV.4.4 Base doping effect on cut-off frequency and maximum oscillation Frequencies	74
IV.4.5 Base doping effect on the forward transit time	75
IV.5 Conclusion	76
References	77
Conclusions	79

LIST OF FIGURES

Figure I.1	Crystal structure of Si and Ge. Unit cell defined by blue atoms.	7
Figure I.2	Germanium band structure.	7
Figure I.3	Band Structure of Si calculated by pseudo-potential technique.	8
Figure I.4	PN junction; a- unbiased, b- forward biased, c- reverse biased.	10
Figure I.5	Components of npn BJT current.	11
Figure I.6	Distribution of minority carriers; in the emitter (left) and in the base (right).	12
Figure I.7	Si BJT and graded SiGe HBT energy band diagrams.	15
Figure I.8	AC current gain to determine cut-off frequency.	16
Figure I.9	Cut-off frequency as a function of Collector current.	17
Figure I.10	Measure of the forward transit time of a bipolar transistor.	18
Figure I.11	Extrinsic and intrinsic resistances in a bipolar transistor.	20
Figure I.12	Depletion capacitances in a bipolar transistor.	21
Figure I.13	A schematic diagram of tensile and compressive strained films	22
Figure I.14	Critical thickness against germanium fraction for pseudomorphic SiGe layers grown on bulk Si (100)	23
Figure II.1	Transport models hierarchy.	27
Figure II.2	Dependant concentration mobility of electrons in Si at 300K	37
Figure II.3	Dependant concentration mobility of holes in Si at 300K	
Figure III.1	Inputs and outputs in Atlas.	44
Figure III.2	Command groups in Atlas.	45
Figure III.3	ATLAS mesh creation.	46
Figure III.4	Gaussian doping profile.	48
Figure III.5	Run-time output window for materials properties.	54
Figure III.6	Run-time output window for calculation.	55
Figure IV.1	Simulated SiGe HBT structure.	60
Figure IV.2	Germanium profile and doping used in the widths simulation.	61
Figure IV.3	Band diagram for SiGe HBT1 to HBT7 in comparison with the Si BJT using the EB model; dimensions are arbitrary.	62
Figure IV.4	DC current gain versus base-emitter voltage.	63
Figure IV.5	Gummel plots according to the EB simulation.	64
Figure IV.6	AC current gain versus frequency to determine the cutoff frequency f_T .	65

LIST OF FIGURES

Figure IV.7	Unilateral power gain versus frequency to determine f_{MAX} .	66
Figure IV.8	Transit time versus inverse of collector current obtained using DD and EB models.	67
Figure IV.9	Germanium profiles and doping used in the trapezoidal shape simulation.	68
Figure IV.10	DC current gain versus base-emitter voltage.	69
Figure IV.11	EB simulation gummel plots.	70
Figure IV.12	The cut-off frequency f_T .	71
Figure IV.13	The unilateral power gain against frequency to determine f_{MAX} .	71
Figure IV.14	DC current gain versus base-emitter voltage.	73
Figure IV.15	EB simulation gummel plots.	73
Figure IV.16	The cut-off frequency f_T .	74
Figure IV.17	The unilateral power gain against frequency to determine f_{MAX} .	74
Figure IV.18	Transit time versus inverse of collector current obtained using EB model.	75

LIST OF TABLES

Table II.1	Bandgap narrowing parameters.	33
Table II.2	Silicon default values.	34
Table II.3	Silicon default values for equations II-43, 44, 45.	34
Table II.4	Parameters for equations II-46 and II-47.	36
Table II.5	Parameters for equations II-51 and II-52.	37
Table II.6	Parameters for equation II-58.	39
Table IV.1	Emitter and collector widths for the seven studied HBTs.	60
Table IV.2	The current gain values obtained for the seven simulated devices.	63
Table IV.3	Cut-off and maximum oscillation frequencies values obtained for the seven simulated devices.	66
Table IV.4	Results of τ_{F0} for the seven devices.	67
Table IV.5	Results of β_F for the three devices HBT1, HBT2 and HBT3.	70
Table IV.6	Results of f_T and f_{MAX} for the three devices HBT1, HBT2 and HBT3.	72
Table IV.7	Results of β_F , f_T and f_{MAX} for the three devices HBT1, HBT2 and HBT3.	75

LIST OF ACRONYMS

<i>BJT</i>	Bipolar junction transistor
<i>HBT</i>	Heterojunction bipolar transistor
Silvaco	Silicon valley corporation
TCAD	Technology computer aided design
DDM	drift-diffusion model
EBTM	energy balance transport model
BTE	Boltzmann transport equation
HEMT	High electron mobility transistor
RF	Radiofrequency
1D	one-dimensional
2D	two-dimensional
DC	Direct current
AC	Alternative current
RADAR	RAdio Detecting And Ranging

LIST OF Symbols

I_{rg}	recombination current in the base
I_{ne}	Electron diffusion current at the emitter edge of the base
I_{nc}	Electron diffusion current at the collector edge of the base
I_{rb}	Recombination current in the base
I_{pe}	Hole diffusion current in the emitter
I_E	The emitter current
I_C	The collector current
I_B	The base current
J_n	Electron current density
J_p	Hole current density
W_E	The emitter width
$P_e(0)$	the hole concentration at the emitter/base depletion region edge
P_{eo}	the hole concentration at the emitter contact
A	Lattice constant
A	Area of the emitter/base junction
β_F	Forward common emitter current gain
B	Common emitter current gain
C_{JE}	Emitter/base depletion capacitance
C_{JC}	Base/collector depletion capacitance
D_n	Diffusion coefficient of electrons
D_p	Diffusion coefficient of holes
D_{nb}	Diffusion coefficient of electrons in the base
ΔE_c	Conduction band discontinuity in a heterojunction
ΔE_V	Valence band discontinuity in a heterojunction
ΔE_G	Bandgap narrowing due to germanium in the base
Δegb	Apparent bandgap narrowing in the base
ΔE_{ge}	Apparent bandgap narrowing in the emitter
E	Electric field
E_F	Fermi level
E_{Fn}	Electron quasi-Fermi level
E_{Fp}	Hole quasi-Fermi level
E_C	Energy level of the conduction band
E_V	Energy level of the valence band
E_G	Semiconductor bandgap
E_i	Intrinsic fermi level
ϵ_0	Permittivity of free space
ϵ_r	Relative permittivity or dielectric constant of silicon
f_T	Cut-off frequency
f_{TMAX}	Peak value of the cut-off frequency
f_{MAX}	Maximum oscillation frequency
G_m	Transconductance
L_n	Electron diffusion length

LIST OF SYMBOLS

L_p	Hole diffusion length
L_{nb}	Electron diffusion length in the base
L_{pe}	Hole diffusion length in the emitter
L_b	Length of the extrinsic base region of a bipolar transistor
L_c	Length of the buried layer of a bipolar transistor
L_e	Length of the emitter of a bipolar transistor
m^*	Electron effective mass
m^*	Hole effective mass
μ_n	Electron mobility
μ_p	Hole mobility
N_a	Acceptor concentration
N_d	Donor concentration
N_{ab}	Acceptor concentration in the base
N_{dc}	Donor concentration in the collector
N_{de}	Donor concentration in the emitter
N_{deff}	Effective doping concentration, including the effects of bandgap narrowing
N_C	Effective density of states in the conduction band
N_V	Effective density of states in the valence band
N	Electron concentration
N_b	Electron concentration in the base
N_i	Intrinsic carrier concentration
n_{bo}	Equilibrium electron concentration in the base
N_{ie}	Intrinsic carrier concentration in a heavily doped emitter
N_{ib}	Intrinsic carrier concentration in a heavily doped base
P	Hole concentration
P_e	Hole concentration in the emitter
p_{eo}	Equilibrium hole concentration in the emitter
Q	Charge on an electron
R_B	Base resistance
R_{BI}	Intrinsic base resistance
R_{BX}	Extrinsic base resistance
R_C	Collector resistance
R_E	Emitter resistance
R_{SBI}	Sheet resistance of the intrinsic base
R_{SBX}	Sheet resistance of the extrinsic base
R_{SBL}	Sheet resistance of the buried layer
T	Temperature
T_n	Electron lifetime
T_p	Hole lifetime
T_{nb}	Electron lifetime in the base
τ_F	Forward transit time
τ_E	Emitter delay

LIST OF SYMBOLS

τ_{EBD}	Emitter/base depletion region delay
τ_B	Base transit time
τ_{CBD}	Collector/base depletion region transit time
V_{BE}	Base/emitter voltage
V_{CE}	Collector/emitter voltage
G_n	electrons generation rate
R_n	recombination rate for electrons
G_p	holes generation rate
R_p	recombination rate for holes
\vec{S}_n	density of energy flux for electrons
\vec{S}_p	density of energy flux for holes
D_n	electrons thermal diffusivity
D_p	holes thermal diffusivity
K_n	electrons thermal conductivity
K_p	holes thermal conductivity

INTRODUCTION

INTRODUCTION

In 1948 the bipolar junction transistor (BJT) was invented at Bell Telephone Laboratories [1-2], ahead of the MOS field-effect transistor (MOSFET) by a decade. The BJT's early dominance had been eroded by the high-density and low-power advantages which show the MOS technology. In some high-frequency and analog applications, BJTs are still preferred regarding high speed, low noise, and high output power advantages such as in some circuits of cell phone amplifier. In some applications, a small number of BJTs are integrated into a high-density complementary MOS (CMOS) chip. This integration between BJT and CMOS is known as the BiCMOS technology [3].

Numerous techniques have been proposed aiming the improvement of bipolar transistor performance, one of them is the introduction of a grading germanium into the silicon base [4-5]. This combining idea of silicon and germanium for use in bipolar transistor engineering is old and just in 1987 the first SiGe hetero-structure bipolar transistor (HBT) was reported [6]. In the 1990s with the revolution in bipolar transistor design, SiGe HBTs have emerged as serious contenders for analog, digital and mixed signal RF application [7]. Previously, hetero-junction bipolar transistors had only been available in compound semiconductor technologies, such as AlGaAs/GaAs [7]. Since the 1990s, with the technology rapid progress used for manufacturing silicon germanium based heterojunction bipolar transistors (SiGe HBTs), these latter have gradually replaced the III-V compound devices technology for their typical applications [8]. This is mainly due to the high performances reached by SiGe based devices, and the compatibility between the SiGe and silicon materials which allows to build them in a conventional substrate beside CMOS circuits (BiCMOS technology), keeping similar cost of manufacturing [9].

The formation of an effective hetero-junction requires two semiconductors with similar lattice spacing. Si and Ge have a relatively large lattice mismatch of 4.2%, so it is very difficult to form a hetero-junction between Si and SiGe without misfit dislocations at the interface. Fortunately, however, in the 1980s a good hetero-junction was obtained with thin SiGe layers and low Ge content (relatively below 30%) [10]. In these cases, the SiGe layer grows under strain so that it fits perfectly onto the silicon lattice without the generation of misfit dislocations. The vital technology breakthrough that led to the emergence of the SiGe is the epitaxial growth of reproducible strained or pseudomorphic SiGe. Strain somehow leads to enhance transport properties and this is caused by changes in band structure [11]. Introduction of carbon in the base is an additional way to improve 1D doping profile preventing the base

dopant from diffusion [12]; reducing the emitter width gives enhancements in SiGe HBTs frequencies[13]; changing the material properties improve the carrier transport. Nowadays, the market for SiGe HBTs has grown rapidly to satisfy the demand for applications such as wireless communications, high-data-rate wireline and automotive radar [14].

The advanced SiGe heterojunction bipolar transistor device is obtained by the addition of germanium (Ge) during the growth; to the silicon base region. Germanium incorporation causes a reduction in the bandgap, leading to a transit time reduction in the base. The advantage of SiGe heterojunction bipolar transistors is the very high frequency response. SiGe HBTs perform well at both room and low temperature conditions [15].Recently, SiGe HBTs with cut-off frequencies f_T of 300 GHz and maximum oscillation frequencies f_{MAX} of 500 GHz were demonstrated [14, 16, 17].

This work is a simulation study of the effect of emitter and intrinsic collector widths on performance of NPN SiGe HBT focusing on the dc current gain, the cut-off frequency, maximum oscillation frequency and the forward transit time. To show the widths effects, seven SiGe HBTs devices of existing architectures were proposed then investigated by ATLAS from SILVACO T-CAD using drift diffusion (DD) and energy balance (EB) models.

The thesis is divided into four chapters as follows:

- Chapter one describes the BJT and SiGe HBT theory.
- Chapter two shows the Si, Ge and SiGe properties.
- Chapter three is reserved for the software used in the present work, namely SILVACO T-CAD
- Chapter four presents the simulation results for the seven proposed devices with their corresponding analysis and discussions.

REFERENCES

- [1] Shockley, W.: circuit element utilizing semiconductive material. US Patent, **2,569,347**, (1951)
- [2] Kroemer, H.: Der Drifttransistor. Naturwissenschaften **40**, 578-579 (1953)
- [3] Alvarez, A.R.: BiCMOS-has the promise been fulfilled. IEEE IEDM Tech. Dig. pp. 355–358 (1991)
- [4] AL-SA'DI, M.: TCAD Based SiGe HBT Advanced Architecture. Thesis, Ecole doctorale de sciences physiques et de l'ingénieur, University of BORDEAUX I (2011)
- [5] Salmon, S.L., Cressler, J. D., Jaeger, R.C. Harame, D.L.: The Influence of Ge Grading on the Bias and Temperature Characteristics of SiGe HBT's for Precision Analog Circuits. IEEE Transactions on Electron Devices **47**, 292-298 (2000)
- [6] Maiti, C.K., Armstrong, G.A. Applications of Silicon–Germanium Heterostructure Devices. IOP Publishing Ltd, London (2001) pp. xiii
- [7] Senapati, B., Maiti. C.K., Chakrabati, N.B.: Silicon Heterostructure Devices for RF Wireless Communication. Int'l. Conf. On VLSI Design, Calcutta, pp. 488-491 (2000)
- [8] Böck, J., Schäfer, H., Knapp, H., Zöschg, D., Aufinger, K., Wurzer, M., Boguth, S., Rest, M., Schreiter, R., Stengl, R., Meister, T.: Sub 5 ps SiGe Bipolar Technology. In: IEDM Tech. Dig., pp. 763–766 (2002)
- [9] Andrés, Quiroga.: Investigation and development of advanced Si/SiGe and Si/SiGeC Heterojunction Bipolar Transistors by means of Technology Modeling. Thesis, Institut d'Électronique Fondamentale, Paris-sud university, (2013)
- [10] Matthews, J.W., Blakeslee, A.E.: Defects in epitaxial multilayers. III. Preparation of almost perfect multilayers. J. Cryst. Growth **32**, 265-273 (1976)
- [11] Chidambaram, P.R., Bowen, C., Chakravarthi, S., Machala, C., Wise, R.: Fundamentals of silicon material properties for successful exploitation of strain engineering in modern CMOS manufacturing. IEEE Transactions on Electron Devices **53**, 944-964 (2006)
- [12] Tillack, B., Heinemann, B., Knoll, D., Rücker, H., Yamamoto, Y.: Base doping and dopant profile control of SiGe npn and pnp HBTs. **254**, 6013-6016 (2008)
- [13] Ellinger, F., Rodoni, L.C., Sialm, G., Kromer, C., von Büren, G., Schmatz, M., Menolfi, C., Toifl, T., Morf, T., Kossel, M., Jäckel, H.: 30-40 GHz drain pumped passive down mixer MMIC fabricated on digital SOI CMOS technology. IEEE Transactions on Microwave Theory and Techniques **52**, 1382-1391 (2004)

- [14] Rücker, H., Heinemann, B., Fox, A.: Half-terahertz SiGe BiCMOS technology. In: IEEE 12th Topical Meeting on Silicon Monolithic Integrated Circuits in RF Systems, pp. 133–136 (2012)
- [15] Woods, B.O.: Device Characterization and Compact Modeling of the SiGe HBT in Extreme Temperature Environments. Thesis, University of Arkansas, Fayetteville, (2013)
- [16] Heinemann, B., Barth, R., Bolze, D., Drews, G., Fischer, G.G., Fox, A., Fursenko, O., Grabolla, T., Haak, U., Knoll, D., Kurps, R., Lisker, M., Marschmeyer, S., Rücker, H., Schmidt, D., Schmidt, J., Schubert, M.A., Tillack, B., Wipf, C., Wolansky, D., Yamamoto, Y.: SiGe HBT technology with f_T/f_{MAX} of 300/500 GHz and 2.0 ps CML gate delay. In: IEEE International Electron Devices Meeting (IEDM), pp. 688–691 (2010)
- [17] Chevalier, P., Meister, T.F., Heinemann, B., Huylenbroeck, S.V., Liebl, W., Fox, A., Sibaja-Hernandezl, A., Chantre, A.: Towards THz SiGe HBTs. In: IEEE Bipolar/BiCMOS Circuits and Technology Meeting (BCTM), pp. 57–65 (2011)

Chapter I

SILICON BIPOLAR AND SILICON-

GERMANIUM HETERO-JUNCTION

BIPOLAR TRANSISTORS PRINCIPLES

I.1 Introduction

The transistor is considered as one of the most important inventions in the last century. Before its invention, electronics were expensive and limited in applications. In the fifties, transistors affected hugely electronics field.

The transistor was invented in 1947 at Bell Telephone Laboratories by physicists John Bardeen, Walter Brattain, and William Shockley. In 1947, Bardeen and Brattain designed a solid-state amplification circuit whose key components were a slab of germanium and two gold point contacts just fractions of a millimeter apart. Brattain discovered that putting a ribbon of gold around a plastic triangle, slicing it through at one point, and pressing the point of the triangle gently down onto the germanium created a dramatic amplification of electric current. Thus was the first point-contact transistor made. But two months later, Shockley stunned Bardeen and Brattain with a significantly improved design. It consisted of three semiconductor layers stacked together, with current flowing through the semiconductor material instead of along the surface. As voltage on the middle layer was adjusted up and down, it could turn current in the three-layer "sandwich" on and off at will. Introduced in 1949, the solid-state transistor could amplify an electrical signal much more efficiently than a bulky vacuum tube. It became the building block for all modern electronics and the foundation for microchip and computer technology. For their work, Shockley, Bardeen, and Brattain received the Nobel Prize in physics in 1956. Scientists working at Bell Telephone Laboratories were trying to understand the nature of electrons at the interface between a metal and a semiconductor (Germanium). They realized that by making two point contacts very close to one another, they could make a three terminal device - the first "point contact" transistor [1]. Nowadays, silicon dominates the electronics industry (95% of the semiconductor market uses the silicon) despite the first transistor was based on germanium. This profound market dominance of Si rests on a number of surprisingly practical advantages that Si has over the other numerous semiconductors [2, 3]. Transistors were a vital part of improvements in existing analog systems, such as radios and stereos.

I.2 Elemental semiconductors: silicon and germanium

Silicon is the best-known semiconductor. Together with germanium (Ge), it is the prototype of a large class of semiconductors with similar crystal structures. Si and Ge crystal structure is the same as that of diamond. In this structure each atom is surrounded by four nearest neighbor atoms forming a tetrahedron (each atom is said to be **four-fold coordinated**). These **tetrahedrally bonded** semiconductors form the mainstay of the electronics industry and the cornerstone of modern technology [4].

In electronic devices such as integrated circuits, silicon is the widely used material. This importance of Si over other semiconductors is referred to:

- (i) The facility of passivating the surface by oxidizing it and forming a layer of stable native oxide that causes a reduction of the surface recombination velocity.
- (ii) Its hardness that allows handling large wafers safely.
- (iii) Up to 1100°C, Si thermally stable, that allows high-temperature processing related to diffusion, oxidation and annealing.
- (iv) Its cost which is relatively low.

Silicon shows some limitations that are due to:

- (i) The indirect band gap and its magnitude which limit optoelectronic applications of this material.
- (ii) The carrier mobility which is relatively low.

The indirect energy gap of silicon limits the optoelectronic applications of this material. However, emerging materials based on layers grown on Si substrate appear to be promising in numerous applications.

Heteroepitaxy involves a single crystal layer growth on a substrate of a different material. The objective of heteroepitaxy is to engineer materials and structures with unique properties. SiGe/Si hetero-structures give an example of practical applications of energy-band-gap engineering, which are very attractive since such systems combine highly developed Si-based technology with the benefits derived by Ge incorporation in Si-based devices as in transistors. The smaller energy gap and larger refractive index of SiGe make these hetero-structures also suitable in optoelectronic applications, such as waveguide detectors that can be employed in fiber-optic communication.

The strained layer heteroepitaxy is an important approach in such structures; here, if the layers are sufficiently thin, the lattice mismatch between the dissimilar semiconductors is accommodated by strain, and no misfit dislocations at the interface are generated. As a result, the lattice distortion leads to band structure changes and hetero-junction band offsets allowing flexibility in band-structure engineering. The typical values of the critical thickness in mismatch between Si and Ge and about 100 nm for such a material system are between about 1 nm for pure Ge (note about 4% lattice (i.e., 1 % mismatch)).

I.2.1 Crystal structure

The crystal structure of silicon and germanium is that of diamond. In this structure, each atom is surrounded by 4 close neighbors to form a tetrahedron; Figure I.1.

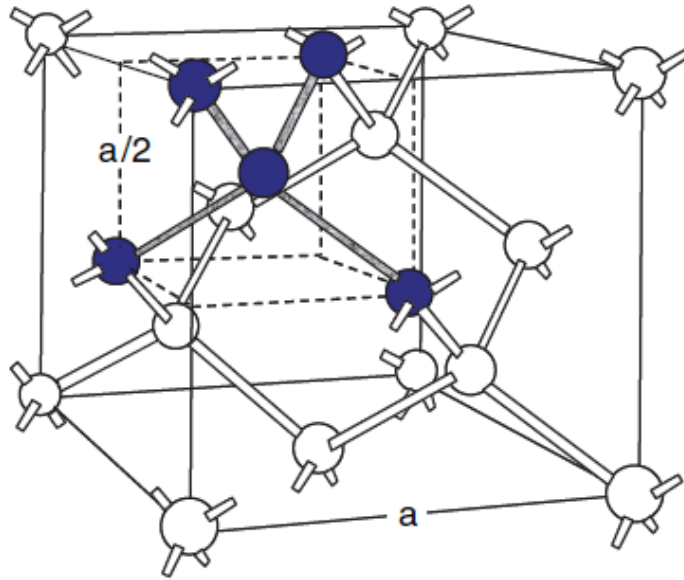


Figure I.1: Crystal structure of Si and Ge. Unit cell defined by bleu atoms [5]

I.2.2 Band structure

Figures I.2 and I.3 illustrate band structures of germanium and silicon, respectively. They were calculated with a sophisticated method known as the pseudo-potential technique. Germanium also has an indirect band structure. The conduction minima are at the L point as presented in Figure I.2. For silicon, the minimum of the conduction band is located close to the X point as shown in Figure I.3. Thus, it is not at the same point in \mathbf{k} -space as the top of the valence band. Such a band structure is called indirect.

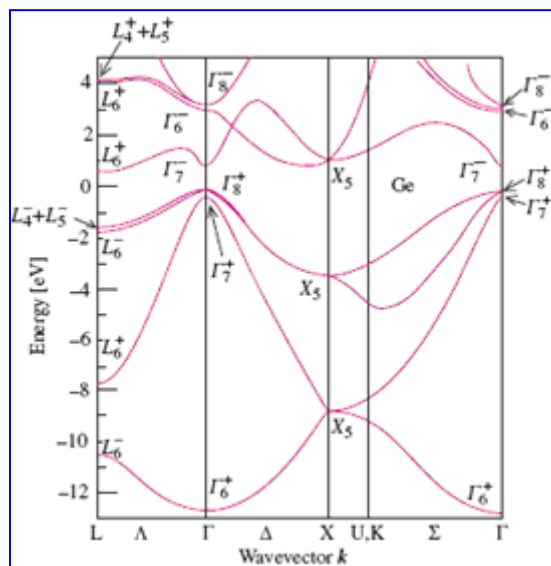


Figure I.2: germanium band structure calculated by pseudo-potential technique [4]

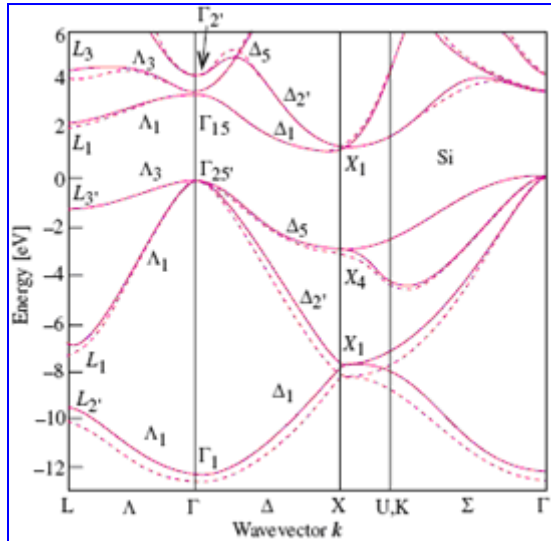


Figure I.3: band Structure of Si calculated by pseudo-potential technique. Solid and dotted lines represent calculations with a nonlocal and a local pseudo-potential, respectively [4]

I.3 PN junction

A PN junction is formed by the juxtaposition of two regions of different types from a semiconductor. When a PN junction is created from the same semiconductor then it is called a PN homo-junction diode. On the other hand, in the case of the creation of a PN junction with two semiconductor materials having different band gaps and different doping impurities, then it is called a PN hetero-junction diode. The difference in densities of donors and acceptors passes from a negative or positive value in the region p to the n-type region. The law of variation of this magnitude depends mainly on the manufacturing technique. Different models can be used to study theoretically the properties of the junction, linear junction, abrupt ...etc. The PN junction is a basic structure in the electronic components and nearly all power devices. The PN junction has a leading role in device structures in a large variety of electronic and photonic devices fabrication. Such as in PN junction structures that used in fabricating switching diodes, solar cells, diode rectifiers, laser diodes (LDs), light emitting diodes (LEDs), tunnel diodes, photodetectors, bipolar junction transistors (BJTs), junction field-effect transistors (JFETs), heterojunction bipolar transistors (HBTs), metal–semiconductor field-effect transistors (MESFETs), high-electron mobility transistors (HEMTs), multi quantum well (MQW) and superlattice (SL) devices. The PN heterojunctions can be created from a wide variety of elemental and compound semiconductors such as n-Si/p-SiGe (as in the present thesis), p-Ge/n-GaAs, n-ZnSe/p-GaAs, p-AlGaAs/n-GaAs, n-InGaAs/n-InP, p-GaN/n-InGaN, p-InAlAs/n-InGaAs, and p-AlGaN/n-InGaN semiconductor heterojunction

devices [6]. In components which are formed of differently doped semiconductors, PN junctions or PN are present at the interfaces. It is therefore essential to understand the physical phenomena that manifest themselves there. The PN junction is also a component in itself. PN junctions conduct current only in one direction of the applied voltage, called forward direction, whereas in the opposite direction, the blocking direction, the current is extremely small. Thus, the function of this component is to let the current flow in one direction. It thus makes it possible to transform an alternating signal into a unipolar signal. This function is widely used in electronic systems or radio frequency detection.

Despite the theoretical description of PN junctions has been fulfilled in 1938 [7], only after the invention of the transistor a full technological significance became obvious with major further advances in theory and technology [8, 9]. In Figure I.4, the application of a positive voltage to the region p with respect to the region n, causes a partial injection of the free electrons in the n-region and the free holes in the p-region toward the junction into the opposite region as excess minority carriers. The PN junction conducts in this condition of bias as shown in Figure I.4 (b). If one applies a negative voltage to the region p with respect to the region n, then both majority carriers types are withdrawn from the junction and cannot be supplied from the adjacent region of opposite conductivity. This is the case of reverse biased PN-junction or blocking direction as shown in Figure I.4 (c).

When the junction is forward biased (a positive voltage is applied on the p-side), there will be a rapid increase in current as the voltage increases. However, when the junction is reverse biased then practically no current flows. The current remains very small with the increase of the reverse bias until reaching a special value known as the critical voltage, at which suddenly the current increases. This sudden increase in current is referred to as the junction breakdown. The direct voltage which is applied on the PN junction is usually less than 1V, whereas, the breakdown voltage varies from few volts to thousands of volts, depending on the device parameters and the dose of doping [10].

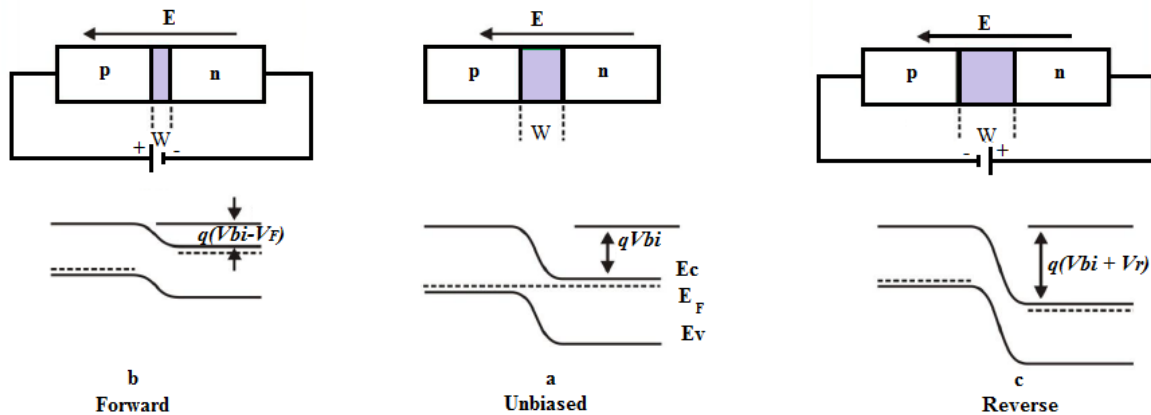


Figure I.4: PN junction; a- unbiased, b- forward biased, c- reverse biased.

I.4 Bipolar junction transistor

The current in a bipolar transistor is caused by holes and electrons transport together, which is not the case in JFETs and MOSFETs (unipolar devices) where current is due to transport of only one type of carrier. Two PN junctions compose a bipolar transistor and hence is called the "**Bipolar Junction Transistor**" (BJT). It exists two types of bipolar transistors: the NPN transistor, where a P-type silicon is located between two N-type regions, and the PNP transistor, where N-type region is sandwiched between two P-type regions. We focus here on the NPN transistor which is presented in Figure I.5. From the NPN transistors, the PNP transistors equations can easily be obtained, provided that the appropriate sign changes are made. The two N-type regions in an NPN transistor are called "emitter" and "collector", and the "base» is reserved to the P region [11].

The illustration shown in Figure I.5 is for a bipolar transistor which operated in the forward active region. The emitter/base and the collector/base junctions are forward biased and reverse biased, respectively. This biasing leads to the injection of electrons into the base and holes into the emitter. During the passage of electrons from the emitter region to the base region, some of them will recombine with holes in the emitter/base depletion region; this is known as the recombination current, I_{rg} . The rest of electrons which reach the base region become minor comparing to holes so they are called minority carriers. The number of minority carriers is more important at the emitter side of the base than the collector side of the base which makes a concentration gradient that encourages them to diffuse towards the collector region [12].

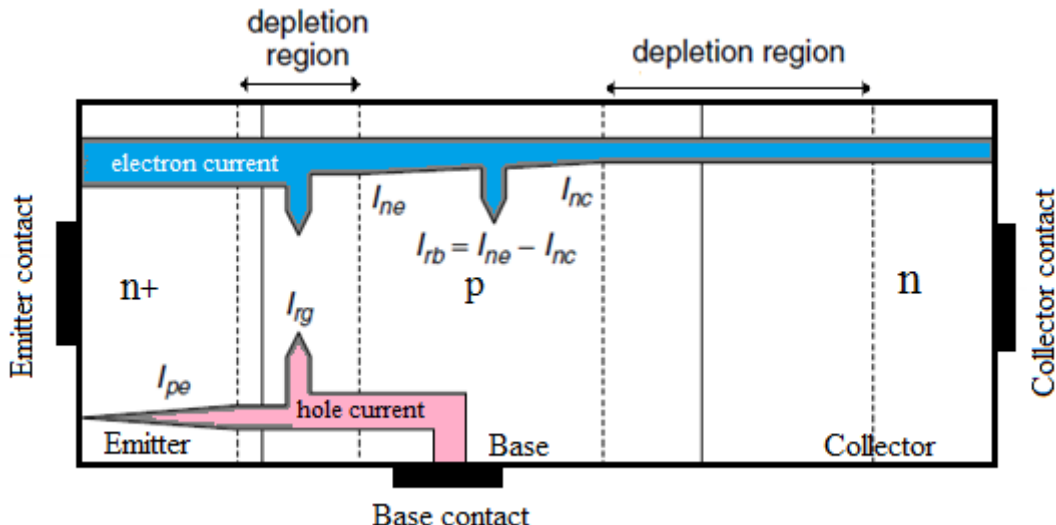


Figure I.5: Components of NPN BJT current

I_{ne} denotes the diffusion current of electrons at the emitter side of the base. When electrons pass through the base region more electrons recombine with holes as a consequence I_{ne} becomes smaller at the collector side of the base so we name it I_{nc} . I_{rb} current is the difference between I_{ne} and I_{nc} currents which denote the recombination current in the base. Due to high electric field across collector/base reverse-biased junction, the recombination in the collector/base depletion region is considered to be negligible. When the electrons attain the collector region they become majority carriers with no recombination.

Concerning the holes as shown in Figure I.5, part of them recombines with electrons in the depletion region of emitter/base and this makes the recombination current I_{rg} . The other part of holes which reach the emitter region becomes minor regarding electrons so they are called minority carriers. These minority carriers diffuse towards the emitter contact and they are called the holes diffusion current I_{pe} .

The emitter, collector and base currents components referring to Figure I.5 are:

$$I_E = I_{ne} + I_{rg} + I_{pe} \quad (\text{I-1})$$

$$I_C = I_{nc} \quad (\text{I-2})$$

$$I_B = I_E - I_C = I_{rb} + I_{rg} + I_{pe} \quad (\text{I-3})$$

I.4.1 Base current

Here, we notice two cases.

a- Thick emitters: the total holes will recombine with electrons in the emitter region as

Figure I.5 illustrates.

b- Thin emitters: a large amount of holes attain the emitter metal contact.

In bipolar transistors I_{pe} which denotes the hole diffusion current is of high importance comparing to other components. The hole distribution in thin emitters is linear as shown in Figure I.6, due to bulk negligible recombination which can be explained by that the hole diffusion length in the emitter is much bigger than the emitter depth w_E . The majority of holes attain the emitter contact.

$$p_e(0) = p_{e0} e^{\frac{qV_{BE}}{kT}} \quad (\text{I - 4})$$

Where $p_e(0)$ is the hole concentration at the emitter/base depletion region edge and p_{e0} is the hole concentration at the emitter contact [4].

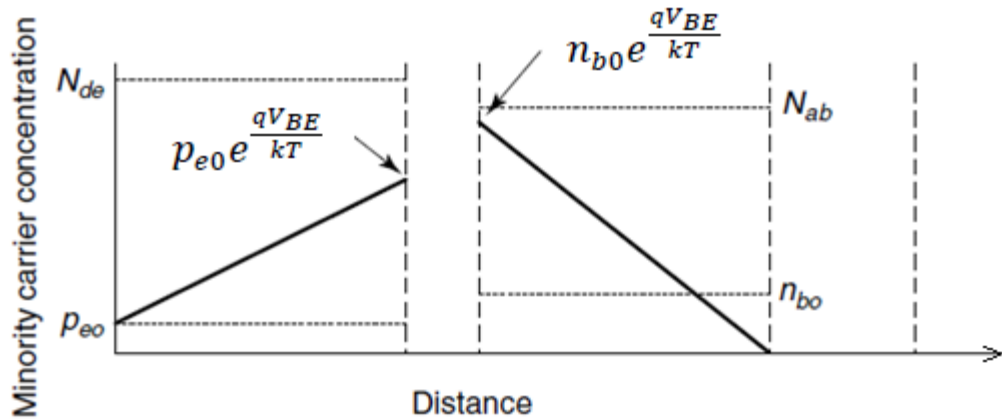


Figure I.6 Distribution of minority carriers; in the emitter (left) and in the base (right)

The base current is written as:

$$J_p = -qD_{pe} \frac{dp_e}{dx} = \frac{qD_{pe}p_{e0}}{W_E} \left(e^{\frac{qV_{BE}}{kT}} - 1 \right) \quad (\text{I - 5})$$

By using:

$$p_{e0}n_{e0} = n_i^2 \quad (\text{I - 6})$$

$$p_{e0}N_{de} = n_i^2 \quad (\text{I - 7})$$

$$p_{e0} = \frac{n_i^2}{N_{de}} \quad (\text{I - 8})$$

By assuming that $V_{be} \gg q/kT$, the base current becomes:

$$I_B = \frac{qAD_{pe}n_i^2}{W_E N_{de}} e^{\frac{qV_{BE}}{kT}} \quad (\text{I - 9})$$

From this expression we notice that the base current is inversely proportional $W_E N_{de}$ in bipolar transistors with thin emitters.

In the case of heavy doping:

$$I_B = \frac{qAD_{pe}n_{i0}^2}{W_E N_{deff}} e^{\frac{qV_{BE}}{kT}} \quad (I - 10)$$

If emitters are so deep, the base current expression becomes:

$$I_B \approx \frac{qAD_{pe}n_i^2}{L_{pe}N_{de}} e^{\frac{qV_{BE}}{kT}} \quad (I - 11)$$

In this case the holes diffusion length L_{pe} is much smaller than emitter depth W_E which causes the recombination of all holes before reaching the emitter contact.

I.4.2 Collector current

The high-speed bipolar transistors need the electrons to cross the base so rapidly. This can be achieved by making the base-width as small as possible. The base width reduction leads to achieve $W_B \ll L_{nb}$ making a linear distribution of electrons in the base, as shown in Figure I.6. At the edge of emitter/base depletion region, the concentration of electrons is:

$$n_b(0) = n_{b0} e^{\frac{qV_{BE}}{kT}} \quad (I - 12)$$

At the edge of collector/base depletion region, the electrons concentration is:

$$n_b(W_B) = n_{b0} e^{\frac{-qV_{CB}}{kT}} \approx 0 \quad (I - 13)$$

For a linear electron distribution across the base, the diffusion current is:

$$J_n = qD_{nb}(\text{gradient of } n_b) = qD_{nb} \left(\frac{n_{b0} e^{\frac{qV_{BE}}{kT}}}{W_B} \right) \quad (I - 14)$$

$$= \frac{qD_{nb}n_{b0}}{W_B} e^{\frac{qV_{BE}}{kT}} \quad (I - 15)$$

By using:

$$p_{b0}n_{b0} = n_i^2 \quad (I - 16)$$

$$N_{ab}n_{b0} = n_i^2 \quad (I - 17)$$

$$n_{b0} = \frac{n_i^2}{N_{ab}} \quad (I - 18)$$

The collector current becomes:

$$I_C = \frac{qAD_{nb}n_i^2}{W_B N_{ab}} e^{\frac{qV_{BE}}{kT}} \quad (I - 19)$$

This expression shows that the collector current is inversely proportional to $W_B N_{ab}$ product.

In the case of heavy doping:

$$I_C = \frac{qAD_{nb}n_{i0}^2}{W_B N_{a\text{eff}}} e^{\frac{qV_{BE}}{kT}} \quad (\text{I - 20})$$

I.4.3 Current gain

In a bipolar transistor, the current gain is calculated by the ratio of collector to base currents.

By using the precedent equations of both collector and base currents, one deduces:

$$\beta = \frac{D_{nb}W_E N_{de}}{D_{pe}W_B N_{ab}} \quad (\text{I - 21})$$

In the case of heavy doping:

$$\beta = \frac{D_{nb}W_E N_{deff}}{D_{pe}W_B N_{a\text{eff}}} \quad (\text{I - 22})$$

From this equation it is clearly noticed that the gain depends on the doping and widths of both emitter and base regions. If a high current gain is desirable, the width of the emitter must be larger than the base one and the doping concentrations of the emitter should be higher comparing to base doping concentration.

I.5 Silicon-Germanium Hetero-junction Bipolar Transistors

The concept of combining silicon and germanium into an alloy for use in high speed transistor engineering is an old one, and was envisioned by Kroemer in his early research on drift transistors discussed above [2, 13]. The Silicon-Germanium hetero-junction bipolar transistor (SiGe HBT) has occupied an important place in electronics nowadays. It features high speed, low noise, and high linearity in comparison with Si BJT and Si CMOS, making SiGe HBT technology more attractive and suitable to the design of ICs. The bipolar transistors (BJT) design requires trade-offs between numerous mechanisms. Achievement of a fast base transit time, and hence a high cut-off frequency value needs a very small base width which is limited by the punch-through mechanism, and this occurs when the emitter/base and collector/base depletion regions intersect in the base region. Increasing the base doping concentration has consequence thinner depletion regions. High base doping degrades the current gain. The main issue that limits the maximum achievable cut-off frequency of Si BJT is the trade-off between current gain and base transit time.

The bandgap engineering technology principle makes the fundamental SiGe HBT advantageous over conventional Si BJT. Several key figure-of-merits could be improved by this bandgap engineering technology. Germanium addition in the SiGe HBT base causes a lowering of the conduction band as illustrates Figure I.7. Various practical Ge profiles designs are possible (box, triangular and trapezoid). The Figure I.7 illustrates the differences between

Si BJT and SiGe HBT regarding their energy band diagram. Apart from the Ge in the base of the SiGe HBT, all the perimeters and doping are the same for both devices. [12-18].

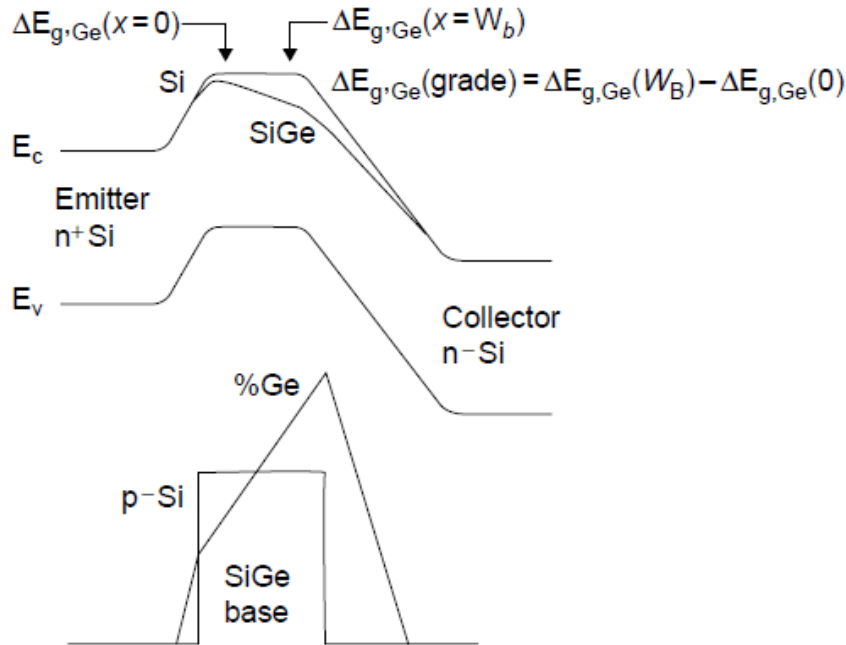


Figure I.7: Si BJT and graded SiGe HBT energy band diagrams

I.5.1 Current gain

If the germanium profile is linearly graded and the doping profile in the base is uniform, the collector current equation of SiGe HBT graded-base is therefore [18]:

$$I_C = \frac{qA\overline{D_{nb}}n_{i0}^2}{W_B N_{AB}} e^{\frac{qV_{BE}}{kT}} e^{\frac{\Delta E_{gb}((N_C N_V D_{nb})SiGe)}{(N_C N_V D_{nb})Si}}} \times \frac{\Delta E_{G(grade)}}{kT} \times \frac{e^{(\Delta E_{G(0)}/kT)}}{1 - e^{-(\Delta E_{G(grade)}/kT)}} \quad (I - 23)$$

$\Delta E_{G(0)}$ denotes the narrowing in the bandgap caused by germanium introduction at the emitter end of the base and $\Delta E_{G(WB)}$ the bandgap narrowing at collector end of the base, $\Delta E_{G(grade)}$ is the base germanium grading which equals to $\Delta E_{G(WB)} - \Delta E_{G(0)}$. D_{nb} is the SiGe graded base average diffusivity of electrons.

The introduction of germanium in the base of Si-BJT leads to an enhancement in the dc current gain of SiGe HBT which is given as:

$$\frac{\beta_{SiGe}}{\beta_{Si}} = \frac{\frac{(N_C N_V \overline{D_{nb}})SiGe}{(N_C N_V D_{nb})Si} \frac{\Delta E_{G(grade)}}{kT} e^{\Delta E_{G(0)}/kT}}{1 - e^{\frac{-\Delta E_{G(grade)}}{kT}}} \quad (I - 24)$$

This expression shows that the enhancement is proportional with both $\Delta E_{G(0)}$ and $\Delta E_{G(WB)} - \Delta E_{G(0)}$ leads to an exponentially enhancement while $\Delta E_{G(grade)}$ leads a linearly enhancement. From the precedent remarks one can notice that the triangular profile of germanium in the

base gives a small current gain whereas a germanium box profile gives a significant gain enhancement.

I.5.2 The transit time

The base transit time Si BJT is:

$$\tau_{B,si} = \frac{W_B^2}{2D_{nb}} \quad (I - 25)$$

In SiGe HBT graded base, the transit time is given as [18]:

$$\tau_B = \frac{W_B^2}{D_{nb}} \frac{kT}{\Delta E_{G(grade)}} \chi \left[1 - \frac{kT}{\Delta E_{G(grade)}} \left(1 - e^{-\frac{\Delta E_{G(grade)}}{kT}} \right) \right] \quad (I - 26)$$

The following equation gives the SiGe HBT graded-base transit time in comparison with Si BJT:

$$\frac{\tau_{BSiGe}}{\tau_{B,si}} = \frac{2kT}{\Delta E_{G(grade)}} \frac{(D_{nb})_{Si}}{(D_{nb})_{SiGe}} \left[1 - \frac{kT}{\Delta E_{G(grade)}} e^{-\frac{\Delta E_{G(grade)}}{kT}} \right] \quad (I - 27)$$

If the germanium grading in the base is finite, the SiGe and Si base transit times ratio is less than unity, and consequently the germanium grading decreases the base transit time and increases the frequency.

I.5.3 Cut-off frequency f_T

The cut-off frequency f_T of a bipolar transistor at which the gain drops to unity (Figure I.8) is considered as the most important parameter at high-frequency.

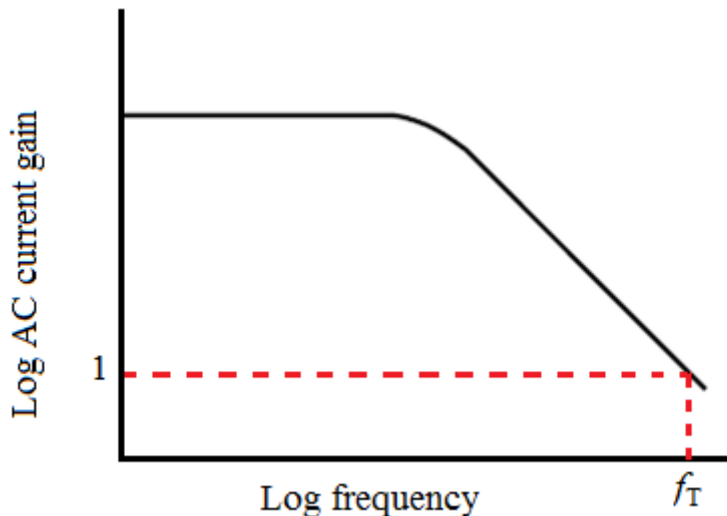


Figure I.8: AC current gain to determine cut-off frequency

For low injection, the SiGe HBT ac figure-of-merit, the cutoff frequency (f_T), can be given as follows:

$$f_T = \frac{1}{2\pi\tau_{ec}} = \frac{1}{2\pi} \left[\frac{kT}{qI_C} (C_{je} + C_{jc}) + \tau_b + \tau_e + \frac{W_{CB}}{2v_{sat}} + r_c C_{jc} \right]^{-1} \quad (\text{I - 28})$$

Where $\frac{qI_C}{kT}$ is the intrinsic transconductance g_m at low injection, C_{je} is emitter-base depletion capacitance, C_{jc} is collector-base depletion capacitances, τ_b is the base transit time, τ_e is the charge storage delay time of emitter, W_{CB} denotes the CB junction space-charge width, v_{sat} is the saturation velocity, and r_c is the dynamic resistance of collector. S-parameter permit the measure of cutoff frequency ($h_{21}=1$), f_T [14]. Equation (I-28) contains τ_{ec} which represents the overall delay time and it controls the bipolar transistor switching speed. Therefore, the presence of SiGe improves τ_b and τ_e leading to an enhancement in both f_T and $f_{T\text{MAX}}$ of the transistor at fixed bias current.

The Figure I.9 illustrates the f_T as a function of collector current. The term of depletion capacitance in equation (I-28) is much larger than the other terms at low currents, which means that f_T increases with I_C . The term of depletion capacitance is small at medium currents comparing to τ_F , and as a consequence f_T stops to increase despite collector current increase reaching a maximal value $f_{T\text{MAX}}$ for f_T :

$$f_{T\text{MAX}} = \frac{1}{2\pi\tau_F} \quad (\text{I - 29})$$

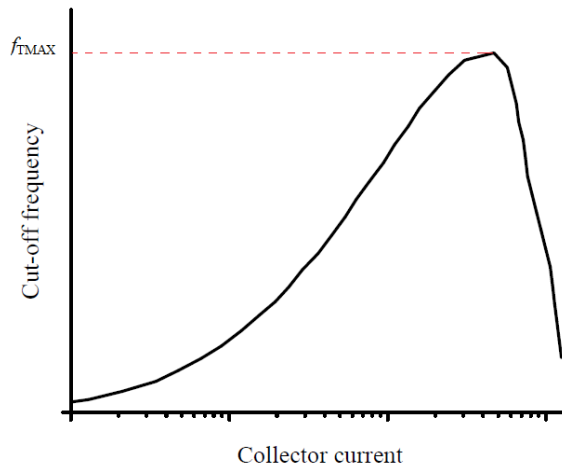


Figure I.9: Cut-off frequency as a function of Collector current

The cut-off frequency decreases obviously at high collector currents and this is caused by high current effects. A clearly defined region of constant f_T is not discernable in many transistors. The graph $\frac{1}{f_T}$ versus $\frac{1}{I_C}$ permits to obtain the forward transit time, as illustrated in

Figure I.10. The interception between the extrapolated straight line and the vertical axis gives τ_F [19]:

$$\tau_F = \frac{1}{2\pi f_I} - R_C C_{jc} \quad (I - 30)$$

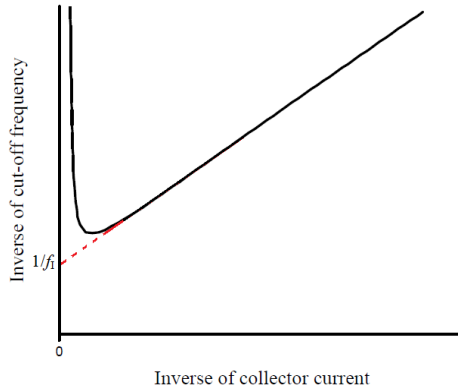


Figure I.10: measure of the forward transit time of a bipolar transistor

I.5.4 Maximum oscillation frequency f_{MAX}

In addition to f_T for a bipolar transistor, there is another important parameter at high-frequency which is called the maximum oscillation frequency f_{MAX} . f_{MAX} is the frequency at which the unilateral power gain of a bipolar transistor drops to unity and is given by:

$$f_{MAX} = \sqrt{\frac{f_T}{8\pi R_B C_{jc}}} \quad (I - 31)$$

From this equation we can notice that f_T , C_{JC} and R_B affect f_{MAX} . The latter two parasitics influence strongly the bipolar circuits' performance, which means that f_{MAX} has a circuit performance prediction better than f_T . Compromising between f_T , C_{JC} and R_B is needed in the design of bipolar transistor.

I.5.5 Base, collector and emitter resistance

The transistor is known by its base, collector and emitter series resistances. The influence of these series resistances at high-frequency performance of the bipolar transistor is remarkable in combination with parasitic capacitances to give RC time constants. The emitter resistance is negligible. f_T is influenced by the combination of collector resistance with the collector/base capacitance as shown in equation (I-28) whereas the combination between the base resistance and the collector/base capacitance influences f_{MAX} as shown in equation (I-31) shows. Thus the performance of bipolar circuits is influenced by such resistances.

I.5.5.1 Base Resistance

The transistor power gain and noise performance is limited by r_b , because it consumes input power and gives rise to thermal noise. As a result, the major challenge in SiGe HBT structural design, fabrication, and process integration is the minimization of the various components of the base resistance. The base resistance is a key parameter in process control and the design of the circuit, and requires careful attention. Therefore, the base resistance is considered as one of the most important electrical parameters of a BJT. The rate at which the input capacitance can be charged is limited by the base resistance and this is why bipolar transistors do not operate at the frequencies predicted by the values of forward transit time. The base resistance is composed by two parts, intrinsic and extrinsic resistances, as illustrated in Figure I.11. The sum of these two parts gives the base resistance. As the same, the collector resistance is composed of three parts and this is due to the resistances of the epitaxial collector, buried layer and collector sink.

R_{Bext} denotes the extrinsic base resistance component extended between the base contact and the edge of the active transistor area. R_{Bext} is calculated from the transistor geometry and the extrinsic base sheet resistance R_{SBext} :

$$R_{Bext} = \frac{R_{SBext} \frac{b_b}{l_b} + R_{CON}}{n_B} \quad (I - 32)$$

R_{CON} denotes the contact resistance and n_B is the number of base contacts. The resistance of the active base region is called the intrinsic base resistance. The active base region which is the region located beneath the emitter. This intrinsic resistance is extracted from the transistor geometry and the intrinsic base sheet resistance:

$$R_{Bint} = C \frac{R_{SBint} \frac{b_e}{l_e}}{n_B^2} \quad (I - 33)$$

The constant C has a value of 1/3 at low currents [20]. The number of base contacts n_B affects considerably the intrinsic base as seen in equation (I-33). If the transistor has only one base contact then the current of the base enters from only one side of the emitter and as a consequence the complete emitter width is the path length for the current flow. In the case of two base contacts, the base current enters from both sides of the emitter, so the path length for the current flow is divided. A further halving of R_{Bint} is caused by the parallel of the two base contacts. Equations (I-32) and (I-33) confirm the reduction of the base resistance in the case of using two base contacts. Unfortunately, the reduction of the intrinsic base resistance is

confronted by the increase in collector/base capacitance, because the need of extra area for the second base contact.

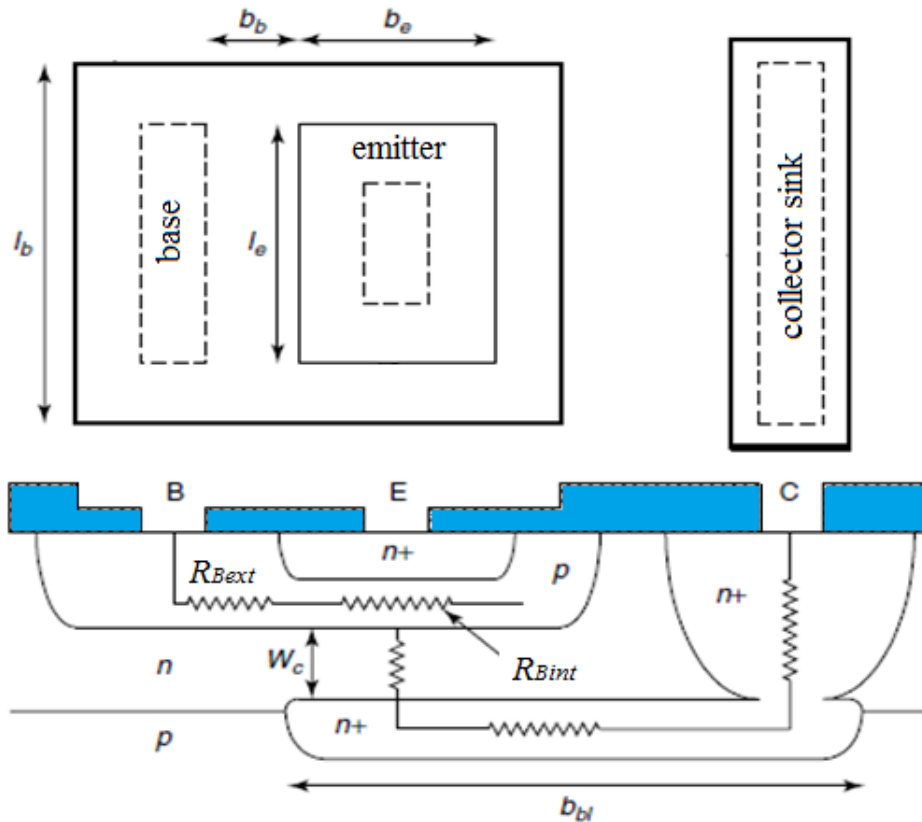


Figure I.11: extrinsic and intrinsic resistances in a bipolar transistor

I.5.5.2 Collector Resistance

In a bipolar transistor, the planar structure causes the appearance of the collector resistance, as presented in Figure I.11. The collector current passes through the collector region towards the surface arriving to the collector contact. The collector resistance is relatively important and this is due to the low amount of doping of the collector. To reach a low collector resistance, one can increase the collector doping. The region below the base is called a buried layer of collector which must be heavily doped. The collector region which is situated under its contact is called the sink helps to reduce the collector resistance. By taking into account the previous procedures in the conception and fabrication of the bipolar transistor has a consequence a low collector resistance. The only impediment is the resistance of the epitaxial collector beneath the base and this is remedied by shrinking this region. Based on the geometry of the transistor and the sheet resistances of the epitaxial collector R_{SC} and the buried layer R_{SBL} , the collector resistance is as follows:

$$R_C = R_{SBL} \frac{b_{bl}}{l_{bl}} + R_{SC} \frac{W_C^2}{l_c b_c} + R_{CC} \quad (I - 34)$$

l_{bl} denotes the length of the buried layer and b_{bl} its width. l_c is the length of the collector region and b_c is its width. R_{CC} is the collector contact resistance.

I.5.6 Emitter/base and collector/base depletion capacitance

The fixed charges in the depletion regions of the emitter/base and collector/base junctions depletion capacitances give rise to capacitances. C_{JE} denotes the emitter/base junction capacitance and C_{JC} denotes the collector/base junction one. Collector/base capacitance has two components, the intrinsic capacitance and the extrinsic one, as illustrated in Figure I.12. The size of the emitter leads to determinate the intrinsic collector/base capacitance whereas the extrinsic capacitance component of collector/base is determined by the space required to make a contact to the base.

For example the emitter/base depletion capacitance is given by:

$$C_{JE} = \frac{C_{JE0}}{\left(1 - \frac{V_{BE}}{V_{JE}}\right)^{M_{JE}}} \quad (I - 35)$$

C_{JE0} is the emitter/base capacitance value at zero bias, V_{JE} is the junction built-in voltage and the factor M_{JE} which can be determined by the emitter profile gradient; $1/2$ for an abrupt profile and $1/3$ for a linearly graded profile.

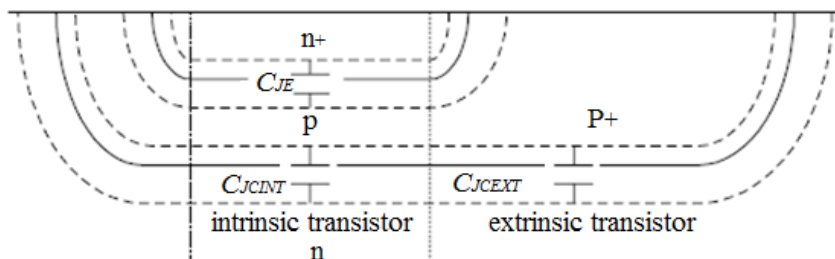


Figure I.12: depletion capacitances in a bipolar transistor

The depletion capacitance has a similar equation.

$$C_{JC} = \frac{C_{JC0}}{\left(1 - \frac{V_{BC}}{V_{JC}}\right)^{M_{JC}}} \quad (I - 36)$$

II.6 Strain, dislocations and critical thickness

In the last decades, the Si/SiGe hetero-structures development permits to engineer band structure and strain which improve the use of Si/SiGe in microelectronic field.

SiGe HBTs show improvements in their operation and this is due to Germanium incorporation in the base. These improvements are confronted by the base maximum Ge amount which is limited by the strain. The thickness of SiGe layer is related to a base Ge amount. Once Ge content is exceeded, misfit dislocation defects will appear due to SiGe relaxation leading to a degradation of the device performance. The germanium lattice constant is larger by 4.2% than the silicon one. For $\text{Si}_{1-x}\text{Ge}_x$ ($0 < x < 1$) relaxed- or bulk- films, the lattice constant as predicted by Vergard's law shows a linearity despite small variations to the measured one. A 10^{-4} nm approximation accuracy is mentioned in [21]:

$$a_{\text{Si}_{1-x}\text{Ge}_x} = 0.5431 + 0.01992x + 0.0002733x^2 (\text{nm}) \quad (\text{I-37})$$

When growing a thin film of $\text{Si}_{1-x}\text{Ge}_x$ on a top of a $\text{Si}_{1-y}\text{Ge}_y$ film, it showed that for $x > y$ the top layer is compressively strained (Figure I-13 (b)) but for $x < y$ the layer is tensile strained (Figure I-13 (d)).

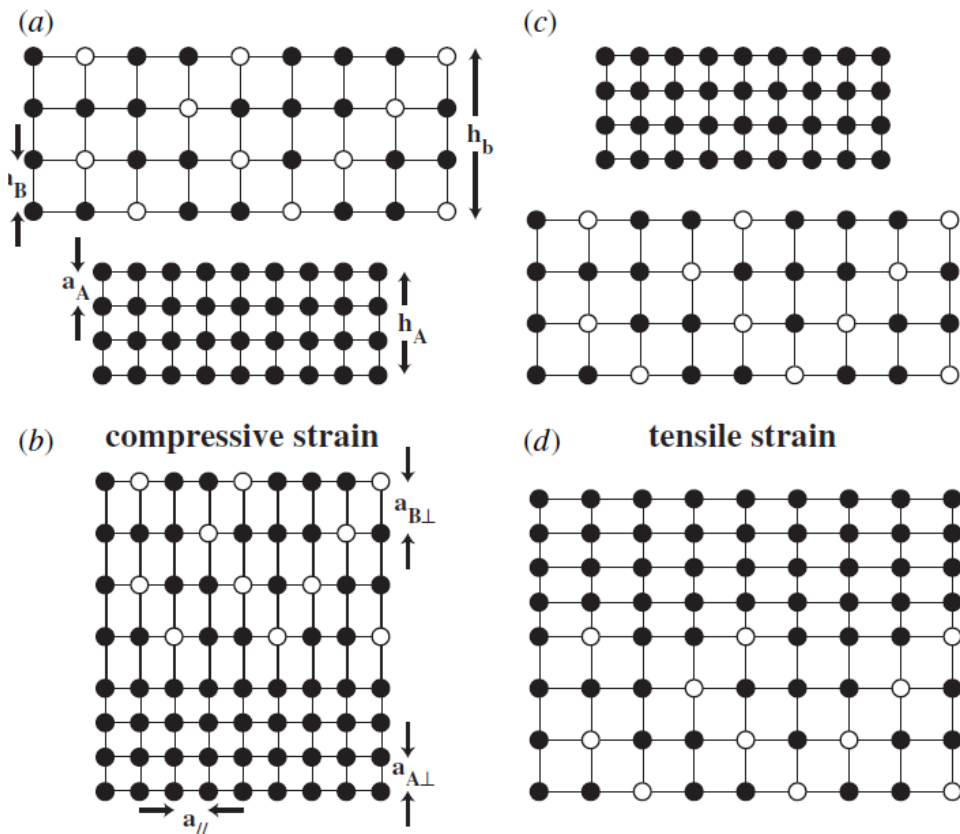


Figure I.13: A schematic diagram of tensile and compressive strained films

The majority hetero-structures of silicon-germanium in electronics field have only one or two strained layers. These strained layers are grown on top of a bulk silicon wafer or a relaxed- $\text{Si}_{1-y}\text{Ge}_y$ virtual substrate which is substantially thicker than the epitaxial layers. If the misfit

between the substrate and an epilayer is sufficiently small, the first grown atomic layers will be strained and lattice matched to the substrate. A hetero-interface pseudomorphic or coherent will be formed in which the strained layer will obliged to take the lattice constant of substrates in-plane and the epilayer becomes tetragonally distorted. When the epitaxial layer thickness is increased, there exists a critical thickness, hc . Additional heterolayers in coherence with the substrate will be elastically strained above hc with the necessity of too much energy. Misfit dislocations defects appear to relieve the epitaxial film strain. The epitaxial layer relaxes and the defects interact with the electrical, optical and thermal properties of the material, causing degradation in the devices performance. The strained epitaxial layer critical thickness prediction is developed by numerous models; van der Merwe [22] and Matthews and Blakeslee [23].

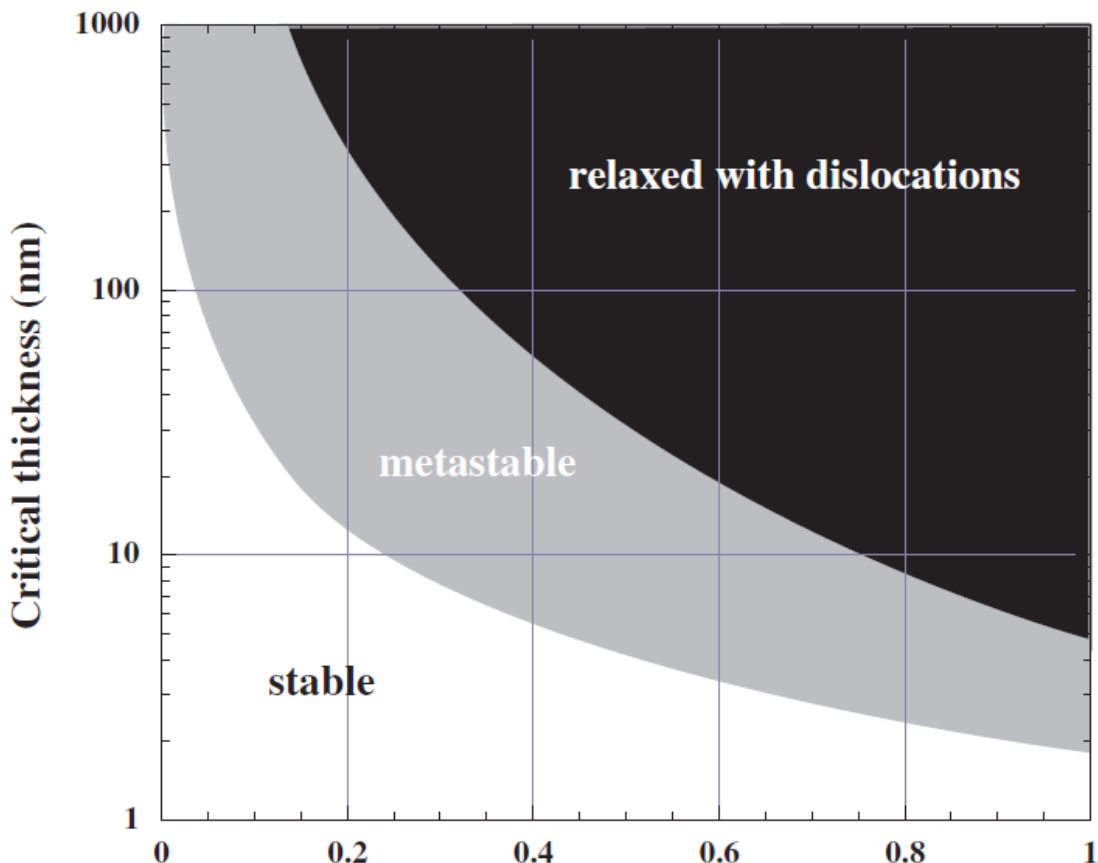


Figure I.14: critical thickness against germanium fraction for pseudomorphic SiGe layers grown on bulk Si (100)

Figure I.14 illustrates the critical thickness and shows the borders of stable and meta-stable regions.

Experiments show that the growth of pseudomorphic layers above the critical thickness is possible. This possibility is partly related to the low densities detection difficulty of dislocations but predominantly related to a kinetic barrier to the relaxation process which allows the meta-stable layers growth.

The threading dislocation segments high density play a role of nucleation centers for strain relaxation and this prevent the growth of meta-stable layers on virtual substrates [24-27].

A cap layer with the same composition as the substrate does not protect the strained layer from relaxation due to cancellation of produced dislocations strain fields.

References

- [1] www.nobelprize.org
- [2] Cressler, J.D.: SiGe HBT technology: A new contender for Si-based RF and microwave circuit applications. *IEEE Transactions on Microwave Theory and Techniques* **46**, 572-589 (1998)
- [3] Fjer M.: Strained Si Heterojunction Bipolar Transistors. Thesis, School of Electrical, Electronic and Computer Engineering, Newcastle University (2011)
- [4] Peter, Y., Cardona, Y.M.: Fundamentals of Semiconductors, Springer. (2005)
- [5] El-Kareh, B.: Silicon Devices and Process Integration. Springer, (2009)
- [6] Li, S.S.: Semiconductor Physical Electronics, second edition. Springer, (2006) pp. 152-158
- [7] Davydov, B.: The rectifying action of semiconductors. *Techn. Phys. UdSSR* **5**, 87–95 (1938)
- [8] Shockley, W.: The theory of p-n junctions in semiconductors and p-n junction transistors. *Bell System Techn. J.* **28**, 435–489 (1949)
- [9] Shockley, W.: The Theory of pn Junctions in Semiconductors. In *Electrons and Holes in Semiconductors*, D. van Nostrand Company Inc, Princeton (1950)
- [10] SZE, S.M., LEE, M.K.: Semiconductor Devices Physics and Technology. 3rd edition, John Wiley & Sons Ltd, USA (2012) pp. 152-158.
- [11] Colinge, J.P., Colinge, C.A.: Physics of Semiconductor Devices. Springer, USA (2002) pp. 152-158
- [12] Ashburn, P.: SiGe Hetero-junction Bipolar Transistors. John Wiley & Sons Ltd, Chichester (2003) pp. 152-158
- [13] Maiti, C.K., Armstrong, G.A.: Applications of Silicon-Germanium Heterostructure Devices. Inst. of Physics Pub. UK (2001) pp. 152-158
- [14] Cressler, J.D., Niu, G.: Silicon-Germanium Heterojunction Bipolar Transistors. Artech House, London (2003)
- [15] Shi, Y.: design and optimization of nano-scaled silicon-germanium heterojunction bipolar transistors. Thesis, faculty of Auburn university, Alabama (2005)
- [16] AL-SA'DI, M.: T-CAD Based SiGe HBT Advanced Architecture Exploration. Thesis, Ecole Doctorale de Sciences Physiques et de l'ingenieur, Bordeau University (2011)
- [17] Cressler, J.D.: Silicon heterostructure handbook. Taylor & Francis Group, USA (2006)

- [18] Harame, D.L., Comfort, J.H., Cressler, J.D., Crabbé, E.F., Sun, J.Y.-C., Meyerson, B.S., Tice, T.: Si/SiGe epitaxial base transistors- part I: materials, physics and circuits. *IEEE Trans. Electron. Devices* **42**, 455-468 (1995)
- [19] Rein, H.M.: Proper choice of the measuring frequency for determining f_T of bipolar transistors. *Solid-State Electron* **26**, 75-82 (1983)
- [20] Roulston, D.J.: Bipolar semiconductor devices. 239, McGraw Hill (1990) pp. 239
- [21] Bublik, V.T.: Gorelik, S.S, Zaitsev, A.A., Polyakov, A.Y.: Calculation of the Binding Energy of Ge-Si Solid Solution. *Physica Status Solidi (b)* **65**, K79-K84 (1974)
- [22] Van der Merwe, J.H.: Crystal Interfaces. Part II. Finite Overgrowths. *Appl. Phys.* **34**, 123-127 (1963)
- [23] Matthews, J.W., Blakeslee, A.E.: Defects in epitaxial multilayers. III. Preparation of almost perfect multilayers. *J. Cryst. Growth* **32**, 265-273 (1976)
- [24] People, R., Bean, J.C.: Calculation of critical layer thickness versus lattice mismatch for $\text{Ge}_x\text{Si}_{1-x}/\text{Si}$ strained-layer heterostructures. *Appl. Phys. Lett.* **47**, 322-324 (1985)
- [25] People, R., Bean, J.C.: Calculation of critical layer thickness versus lattice mismatch for $\text{Ge}_x\text{Si}_{1-x}/\text{Si}$ strained-layer heterostructures. *Appl. Phys. Lett.* **49**, 229 (1985)
- [26] Dobson, B.W., Tsao, J.Y.: Relaxation of strained-layer semiconductor structures via plastic flow. *Appl. Phys. Lett.* **51**, 1325-1327 (1988)
- [27] Dobson, B.W. Tsao, J.Y.: Relaxation of strained-layer semiconductor structures via plastic flow. *Appl. Phys. Lett.* **52**, 852 (1988)

Chapter II

Si AND SiGe PHYSICAL

MODELS

II.1 Introduction

Physical models are needed for bipolar device simulation. In Atlas, the selection of these models is allowed by the MODEL statement. Some default set of bipolar transistor models are implanted in Atlas including: bandgap narrowing (BGN), concentration dependent lifetime (CONSRH), concentration dependent mobility (CONMOB), field dependent mobility (FLDMOB), Fermi statistics (FERMI) and Auger recombination (AUGER). In this chapter, a set of all physical models is presented with full description. Figure II.1 illustrates the hierarchical transport models.

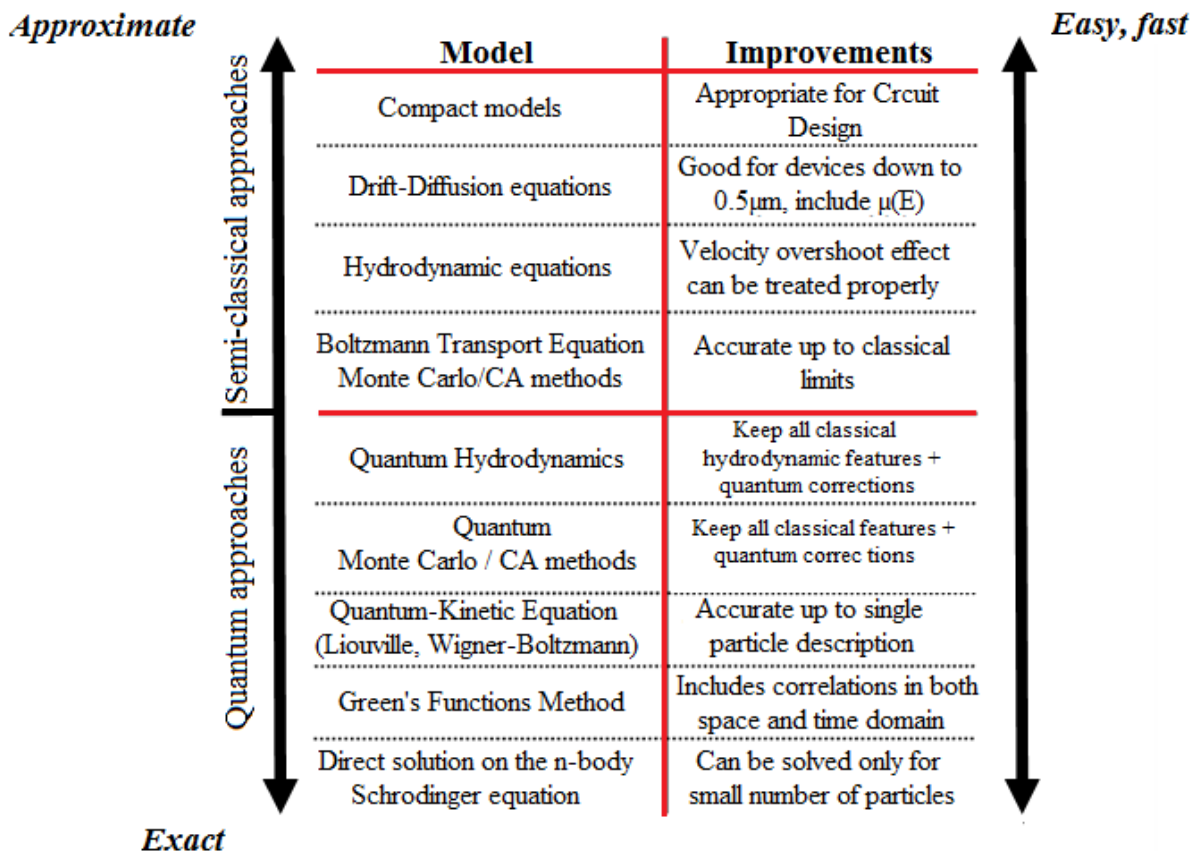


Figure II.1: Transport models hierarchy [1]

III.2 The energy balance model

Derivations based upon the Boltzmann transport equation have shown that the current densities in the continuity equations may be approximated by a drift-diffusion (DD) model so DD is a Boltzmann transport equation (BTE) low-order approximation. This Drift-Diffusion Model is considered as the simplest useful model of carrier transport since no independent variables are added to ψ , n and p . This carrier transport conventional model neglects non-local transport effects such as velocity overshoot, diffusion associated with carrier temperature gradients and dependence of ionization rates on carrier energy distribution. The deep-

submicrometer devices modeling with the DD model becomes progressively problematic with its inaccuracy [2]. Hence, more accurate models named energy balance and hydrodynamic are therefore come to be suitable for simulating deep submicron devices. ATLAS supplies both drift-diffusion, hydrodynamic and energy balance transport models.

As discussed previously, the drift–diffusion approximation can lead to device characteristics inaccuracy prediction, in the case of base width below 30 nm. In this case, the use of energy balance simulation is needed [3]. A higher-order solution to the generalized BTE is necessary to include an additional coupling of the current density to the carrier temperature (energy). Therefore, the energy balance model requires the solution of up to five coupled equations. The energy balance model (EBM) of Stratton is used in SILVACO’s ATLAS software for non-local carrier transport in semiconductors. The relation between the electrostatic potential ψ and the space charge density ρ in Poisson’s equation is given as follows [4]:

$$\operatorname{div}(\varepsilon \nabla \psi) = -\rho \quad (\text{II-1})$$

Where ε is the local permittivity and ∇ is Nabla-operator.

Electrons and holes continuity equations are expressed as follows [4]:

$$\frac{\partial n}{\partial t} = \frac{1}{q} \operatorname{div} \vec{J}_n + G_n - R_n \quad (\text{II-2})$$

$$\frac{\partial p}{\partial t} = -\frac{1}{q} \operatorname{div} \vec{J}_p + G_p - R_p \quad (\text{II-3})$$

Where n and p are the concentrations of electron and hole, \vec{J}_n and \vec{J}_p are the current densities for electrons and holes, G_n and G_p are the electrons and holes generation rates, R_n and R_p are the recombination rates for electrons and holes, and q is the electron charge.

Equations (1), (2) and (3) are used for device simulation. However, more equations are required to specify particular physical models for: \vec{J}_n , \vec{J}_p , G_n , G_p , R_n and R_p .

It was explained in [5, 6] that the drift-diffusion model (DDM) is the simplest model for describing charge transport in semiconductor devices where the non-local transport effects such as velocity overshoot, diffusion associated with carrier temperature gradients, and the dependence of impact ionization rates on carrier energy distributions were neglected. However, in some cases such as the case of low dimensional structures the DDM is not sufficient and more suitable models have to be used in this case, such as the energy balance model. The energy balance transport model (EBTM) refers to the Stratton’s model and its

derivatives based on Boltzmann transport equation (BTE) [4, 7, 8]. The carrier temperature for electrons and holes T_n and T_p are introduced in the EBTM in order to obtain an energy balance equation with the associated equations of current density and energy flux $S_{n,p}$.

The EBTM for electrons can be presented as follows:

$$\operatorname{div} \vec{S}_n = \frac{1}{q} \vec{J}_n \cdot \vec{E} - W_n - \frac{3k_B}{2} \frac{\partial}{\partial t} (\lambda_n^* n T_n) \quad (\text{II-4})$$

$$\vec{J}_n = q D_n \nabla n - q \mu_n n \nabla \psi + q n D_n^T \nabla T_n \quad (\text{II-5})$$

$$\vec{S}_n = -K_n \nabla T_n + \left(\frac{k_B \delta_n}{q} \right) \vec{J}_n T_n \quad (\text{II-6})$$

The Fermi-Dirac statistics is:

$$f(\varepsilon) = \frac{1}{1 + e^{\frac{\epsilon - E_F}{kT_L}}} \quad (\text{II-7})$$

And the EBTM for holes can be expressed as follows:

$$\operatorname{div} \vec{S}_p = \frac{1}{q} \vec{J}_p \cdot \vec{E} - W_p - \frac{3k_B}{2} \frac{\partial}{\partial t} (\lambda_p^* p T_p) \quad (\text{II-8})$$

$$\vec{J}_p = -q D_p \nabla p - q \mu_p p \nabla \psi - q p D_p^T \nabla T_p \quad (\text{II-9})$$

$$\vec{S}_p = -K_p \nabla T_p + \left(\frac{k_B \delta_p}{q} \right) \vec{J}_p T_p \quad (\text{II-10})$$

Where \vec{S}_n and \vec{S}_p are the densities of energy flux for electrons and holes, E is the electric field, k_B is Boltzmann constant, μ_n and μ_p are the electrons and holes mobilities. D_n and D_p are electrons and holes thermal diffusivities. W_n and W_p are electrons and holes rates of energy density loss. K_n and K_p are the electrons and holes thermal conductivities. δ_n and δ_p are other transport coefficient. All these parameters are defined for the electrons and holes as follows:

For electrons:

$$D_n = \frac{\mu_n k T_n}{q} \lambda_n^* \quad (\text{II-11})$$

$$\lambda_n^* = \frac{F(1/2)(\eta_n)}{F-1/2(\eta_n)}, \quad \eta_n = \frac{\epsilon_{Fn} - \epsilon_c}{k T_n} = F_{1/2}^{-1} \left(\frac{n}{N_c} \right) \quad (\text{II-12})$$

$$D_n^T = \left(\mu_{2n} - \frac{3}{2} \lambda_n^* \mu_n \right) \frac{k}{q} = \mu_n \left(\frac{k}{q} \right) (1 + \xi_n) \quad (\text{II-13})$$

$$\mu_{2n} = \mu_n \left(\frac{5}{2} + \xi_n \right) \frac{F_{\xi_n+3/2}(\eta_n)}{F_{\xi_n+1/2}(\eta_n)} \quad (\text{II-14})$$

$$K_n = qn\mu_n \left(\frac{k}{q} \right)^2 \Delta_n T_n \quad (\text{II-15})$$

$$\Delta_n = \delta_n \left[\left(\xi_n + \frac{7}{2} \right) \frac{F_{\xi_n+5/2}(\eta_n)}{F_{\xi_n+3/2}(\eta_n)} - \left(\xi_n + \frac{5}{2} \right) \frac{F_{\xi_n+3/2}(\eta_n)}{F_{\xi_n+1/2}(\eta_n)} \right] \quad (\text{II-16})$$

$$\delta_n = \frac{\mu_{2n}}{\mu_n} \quad (\text{II-17})$$

For holes:

$$D_p = \frac{\mu_p k T_p}{q} \lambda_p^* \quad (\text{II-18})$$

$$\lambda_p^* = \frac{F(1/2)(\eta_p)}{F-1/2(\eta_p)}, \quad \eta_p = \frac{\epsilon_v - \epsilon_{Fp}}{k T_p} = F_{1/2}^{-1} \left(\frac{p}{N_v} \right) \quad (\text{II-19})$$

$$D_p^T = \left(\mu_{2p} - \frac{3}{2} \lambda_p^* \mu_p \right) \frac{k}{q} = \mu_p \left(\frac{k}{q} \right) (1 + \xi_p) \quad (\text{II-20})$$

$$\mu_{2p} = \mu_p \left(\frac{5}{2} + \xi_p \right) \frac{F_{\xi_p+3/2}(\eta_p)}{F_{\xi_p+1/2}(\eta_p)} \quad (\text{II-21})$$

$$K_p = qp\mu_p \left(\frac{k}{q} \right)^2 \Delta_p T_p \quad (\text{II-22})$$

$$\Delta_p = \delta_p \left[\left(\xi_p + \frac{7}{2} \right) \frac{F_{\xi_p+5/2}(\eta_p)}{F_{\xi_p+3/2}(\eta_p)} - \left(\xi_p + \frac{5}{2} \right) \frac{F_{\xi_p+3/2}(\eta_p)}{F_{\xi_p+1/2}(\eta_p)} \right] \quad (\text{II-23})$$

$$\delta_p = \frac{\mu_{2p}}{\mu_p} \quad (\text{II-24})$$

ξ_n and ξ_p are in dependence with the carriers temperature. In the high-field saturated velocity limit, the mobilities of electrons and holes and their temperature are inversely proportional. $\xi_n = \xi_p = -1$ corresponds to the energy balance transport model in which the term of the thermal diffusion in the current density presented in equation (II-5) $qnD_n^T \nabla T_n$ is eliminated (D_n^T in equation II-13 becomes 0).

II.3 SiGe empirical material characteristics

Advances in the growth of Silicon and $\text{Si}_{(1-x)}\text{Ge}_{(x)}$ alloys have allowed the potential for using bandgap engineering to construct heterojunction devices such as HBTs and HEMTs using

these materials. BLAZE supports the SiGe material system by providing composition dependent material parameters. These parameters are accessed by specifying the material name SiGe.

The following sections describe the functional relationship between Ge mole fraction x , and the SiGe material characteristics necessary for device simulation.

II.3.1 Bandgap

Bandgap is one of the most fundamental parameters for any material. For SiGe, the dependence of the bandgap on the Ge mole fraction, x , is divided into ranges as follows [4, 9]:

- for $x \leq 0,245$

$$E_g = 1,08 + \frac{x \times (0,945 - 1,08)}{0,245} \quad (\text{II. 25})$$

- For $0,245 \leq x \leq 0,35$

$$E_g = 0,945 + (x - 0,245) \times \frac{0,87 - 0,945}{0,35 - 0,245} \quad (\text{II. 26})$$

The temperature dependence of the bandgap of SiGe is calculated the same as for Silicon except that $E_{g\alpha}$ and $E_{g\beta}$ are a function of Ge mole fraction x as follows:

$$E_g(T_L) = E_g + E_{g\alpha} \left[\frac{300^2}{300+E_{g\beta}} - \frac{T_L^2}{T_L+E_{g\beta}} \right] \quad (\text{II-27})$$

$$E_{g\alpha} = (4.73 + x \times (4.77 - 4.73)) \times 10^{-4} \quad (\text{II-28})$$

$$E_{g\beta} = 636 + x \times (235 - 636) \quad (\text{II-29})$$

II.3.2 Electron Affinity

The electron affinity of SiGe is taken to be constant (4.17) with respect to composition.

II.3.3 Density of States

The density of states for SiGe is defined differently compared to the previous materials by not being a function of the effective masses. Instead the density of states have been made to depend upon the Ge mole fraction, x composition, according to:

$$N_C = 2,8 \times 10^{19} + x \times (1,04 \times 10^{19} - 2,8 \times 10^{19}) \quad (\text{II-30})$$

$$N_V = 1,04 \times 10^{19} + x \times (6,0 \times 10^{18} - 1,04 \times 10^{19}) \quad (\text{II-31})$$

II.3.4 Dielectric Function

The compositional dependence of the static dielectric constant of SiGe is given by:

$$\epsilon = 11,8 + 4,2 \times x \quad (\text{II-32})$$

II.3.5 Low Field Mobility

SiGe low field mobility at room temperature is given by [10] as:

$$\mu_n \approx (1396 - 4315 \times x)_{\text{cm}^2\text{V}^{-1}\text{s}^{-1}} \quad 0 \leq x \leq 0,3 \quad \text{à } 300\text{K} \quad (\text{II-33})$$

$$\mu_p \approx (450 - 865 \times x)_{\text{cm}^2\text{V}^{-1}\text{s}^{-1}} \quad 0 \leq x \leq 0,3 \quad \text{à } 300\text{K} \quad (\text{II-34})$$

II.3.6 Velocity Saturation

In SiGe, the temperature dependent velocity saturation, used in the field dependent mobility model is defined by the following equations.

$$V_{\text{SATN}} = 1,38 \times 10^7 \cdot \sqrt{\tanh\left(\frac{175}{T_L}\right)} \quad (\text{II-35})$$

$$V_{\text{SATP}} = 9,05 \times 10^6 \cdot \sqrt{\tanh\left(\frac{312}{T_L}\right)} \quad (\text{II-36})$$

II.4 Si and SiGe physical models

Atlas gives some physical models concerning Silicon, poly-silicon and silicon-germanium compound.

II.4.1 Band-gap narrowing

It was shown experimentally that the product $p n$ is doping dependent in silicon, when the doping is above 10^{18} cm^{-3} [11]. If there is an increase in the doping amount, the bandgap narrows. This phenomenon is simulated by a spatially varying intrinsic concentration n_{ie} :

$$n_{ie}^2 = n_i^2 \exp\left(\frac{\Delta E_g}{kT}\right) \quad (\text{II-37})$$

The apparent band gap narrowing in Silicon was presented as empirical expression and this is reported for the first time by Slotboom and de Graaff. This was derived from the collector current measure of an npn transistor (for p-type Si) [12]. The BGN in Si was theoretically predicted by Lanyon and Tuft [13] using the concept of stored electrostatic energy of majority-minority carrier pairs. another empirical expression for the in n-type Si was given by del Alamo *et al.* [14]. This latter expression gave 35mV less than Slotboom and de Graaff expression. Swirhun *et al.* [15] are in agreement with Slotboom and de Graaff in that the apparent BGN is smaller in n-type than in p-type Si.

Klaassen [16] modified the Slotboom and de Graaff model [17]. The expression used in ATLAS is from Slotboom and de Graaf:

$$\Delta E_g = V_1 \left[\ln \frac{N}{V_0} + \sqrt{\left(\ln \frac{N}{V_0} \right)^2 + C} \right] \quad (\text{II-38})$$

V_1, V_0 , and C are defaults values from Slotboom [12] and Klaassen [16] and are shown in Table II.1.

Table II.1: Bandgap narrowing parameters

Parameter	Slotboom	Klaassen
V_1 (eV)	9.10^{-3}	$6.92.10^{-3}$
V_0 (cm $^{-3}$)	1.10^{17}	$1.3.10^{17}$
C	0.5	0.5

The physical models are influenced by the bandgap narrowing due to the amount of doping and this is modeled by subtracting the result of Equation (II-38) from the bandgap, E_g . The electric field is also influenced. The adjustment takes the form:

$$\vec{E}_n = -\nabla \left(\psi + \frac{kT_L}{q} \ln n_{ie} \right) \quad (\text{II} - 39)$$

$$\vec{E}_p = -\nabla \left(\psi - \frac{kT_L}{q} \ln n_{ie} \right) \quad (\text{II} - 40)$$

The effective electron affinity considering the band gap variation is given as follows:

$$\chi_{eff} = \chi + \Delta E_g \times ASYMMETRY \quad (\text{III} - 41)$$

Where ASYMMETRY is a factor. One can specify the value of the asymmetry factor using the ASYMMETRY parameter of the MATERIAL statement in Atlas simulator.

II.4.2 Shockley-Read-Hall (SRH) Recombination

The defect presence in the forbidden gap of a semiconductor activates the phonon transitions. This phenomenon has two steps and was first derived by Shockley and Read [18] and then by Hall [19]. The Shockley–Read–Hall (SRH) and Auger recombination are considered as the most dominant recombination processes in Si bulk [20]. Because of the indirect nature of Si gap, the radiative recombination is considered negligible. The recombination which requires excitons and shallow-level traps needs low temperature.

The Shockley-Read-Hall recombination is modeled as follows:

$$R_{SRH} = \frac{pn - n_{ie}^2}{\tau_{P0}[n + n_{ie} \exp(E_{TRAP}/kT_L)] + \tau_{n0}[P + n_{ie} \exp(-E_{TRAP}/kT_L)]} \quad (\text{II}-42)$$

E_{TRAP} is the difference between E_t and E_i , where E_t is the energy level for the recombination centres, E_i is the intrinsic Fermi energy and n_{ie} is the effective intrinsic carrier concentration including bandgap narrowing effects. The default trap energy level is the intrinsic level, E_i . τ_{n0} and τ_{P0} are the lifetimes of electron and hole, respectively. Table II.2 shows the silicon default values.

Table II.2: Silicon default values

Parameter	Default
$E_T - E_i$ (eV)	0
τ_{n0} (s)	1×10^{-7}
τ_{p0} (s)	1×10^{-7}

II.4.2.1 SRH Concentration-Dependent Lifetime Model

The impurity concentration (doping) affects the constant carrier lifetimes which becomes function of impurity concentration [21, 22, 23]. The SRH recombination model above is then modeled as:

$$R_{SRH} = \frac{pn - n_{ie}^2}{\tau_p[n + n_{ie} \exp(E_{TRAP}/kT_L)] + \tau_n[P + n_{ie} \exp(-E_{TRAP}/kT_L)]} \quad (\text{II - 43})$$

$$\tau_n = \tau_{n0} / \left[A_N + B_N \left(\frac{N_{total}}{N_{SRHN}} \right) + C_N \left(\frac{N_{total}}{N_{SRHN}} \right)^{E_N} \right] \quad (\text{II - 44})$$

$$\tau_p = \tau_{p0} / \left[A_P + B_P \left(\frac{N_{total}}{N_{SRHP}} \right) + C_P \left(\frac{N_{total}}{N_{SRHP}} \right)^{E_P} \right] \quad (\text{II - 45})$$

Where N is the impurity concentration. The τ_{n0} , τ_{p0} , N_{SRHP} , N_{SRHN} , A_N , B_N , C_N , A_P , B_P and C_P are constants as shown in table II.3.

Table II-3: Silicon default values [4]

Parameter	Default value
τ_{n0} (s)	1×10^{-7}
N_{SRHN} (cm^{-3})	5×10^{16}
τ_{p0} (s)	1×10^{-7}
N_{SRHP} (cm^{-3})	5×10^{16}
A_N	1
A_P	1
B_N	1
B_P	1
C_N	0
C_P	0
E_N	0
E_P	0

II.4.3 Field dependent mobility

The electric fields affect the carriers as a consequence they are being accelerated and at the same time they lose momentum because of scattering processes (lattice vibrations, impurity ions, other carriers, interfaces and material imperfection). The latter mechanisms complicate the device modeling; therefore the mobility is considered as a lattice temperature, a local electric field and a doping concentration function.

The mobility is dependent on impurity scattering and phonon (they tend to decrease the low-field mobility) in the region where the field is low. In the high electric field, the mobility decreases. The mean drift velocity rises slowly with the increase of electric field. Finally, the velocity saturates to be called v_{sat} and it is a function of T_L . The characterization of μ_{n0} and μ_{p0} as a function of doping and lattice temperature and the description of the transition between low-field and high-field regions are involved in the case of modeling the mobility in the materials bulk.

In Atlas, one can characterize the low-field mobility as follows: user defined; a carrier scattering model relating mobility to carrier concentration and temperature; a lookup table as a function of doping; an analytic function of doping and temperature [24]; or a unified model dependent on impurity, lattice and carrier–carrier scattering and temperature [25,26]. The unified model dependent on impurity is useful for bipolar device simulation, as it shows excellent agreement with available experimental data.

The velocity of carriers starts to saturate at a high electric field and has to be accounted for by a reduction of effective mobility, because the drift velocity is the mobility and electric field product in the current flow direction. The following expression [27] is used to implement a field-dependent mobility for both holes and electrons, that provides a smooth transition between low-field and high-field behavior.

II.4.4 Low Field Mobility Models

In Blaze (the used software in simulation in this thesis), a default models are implanted and are applicable for the majority of materials in the case of low field mobility;

$$\mu_{n0}(T_L) = \mu_N(T_L/300)^{-T\mu_N} \quad (\text{II-46})$$

$$\mu_{p0}(T_L) = \mu_P(T_L/300)^{-T\mu_P} \quad (\text{II-47})$$

Where T_L is the temperature in degrees Kelvin and the μ_N , μ_P , $T\mu_N$, and $T\mu_P$ parameters are user-definable as shown in Table II.4.

Table II.4: Parameters for equations II-46 and II-47

Parameter	Value
μ_N (cm ² /V.s)	1000
μ_P (cm ² /V.s)	500
$T\mu_N$	1.5
$T\mu_P$	1.5

II.4.4.1 Parallel Electric Field-Dependent Mobility Models

The Standard Mobility and the Negative Differential Mobility Models exist in ATLAS/BLAZE for electric field-dependent mobility. They contain appropriate default values of parameters for several materials. You have the choice to use the mobility type you prefer for each material and alter the material parameter.

By taking into account the saturation velocity, The Standard Mobility Model is defined as follows:

$$\mu_N(E) = \mu_{n0} \left[1 + \left(\frac{\mu_{n0} E}{V_{SATN}} \right)^{\beta_N} \right]^{-1/\beta_N} \quad (\text{II - 48})$$

$$\mu_P(E) = \mu_{p0} \left[1 + \left(\frac{\mu_{p0} E}{V_{SATP}} \right)^{\beta_P} \right]^{-1/\beta_P} \quad (\text{II - 49})$$

Where E is the parallel electric field and μ_{n0} and μ_{p0} are the low-field mobilities of electron and hole, respectively. The parameters $\beta_N = 2$ and $\beta_P = 1$ are user definable. The saturation velocities are temperature dependent and they are given as follows [4]:

$$v_{sat}^n = v_{sat}^p = \frac{2.4 \times 10^7}{1 + 0.8 \exp(T_L/600)} \text{ (cm /s)} \quad (\text{II - 50})$$

In Blaze, the specification of FLDMOB and EVSATMOD=0 in the MODEL statement activates this model.

When the drift velocity of carrier reach maximum value at specific electric field then reduces with the electric field increase, then the Negative Differential Mobility Model of Barnes et. al. [28] is applicable. It is defined as:

$$\mu_n(E) = \frac{\mu_{n0} + \frac{v_{satn}}{E} (E/E_{0N})^{\gamma_N}}{1 + (E/E_{0N})^{\gamma_N}} \quad (\text{II - 51})$$

$$\mu_p(E) = \frac{\mu_{p0} + \frac{v_{satp}}{E} (E/E_{0P})^{\gamma_P}}{1 + (E/E_{0P})^{\gamma_P}} \quad (\text{II - 52})$$

v_{satn} and v_{satp} are the saturation velocities of the electron and hole, μ_{n0} , μ_{p0} are the mobilities of electron and hole at low-field, the default parameters of previous equation are listed in table II.5. The specification of EVSATMOD=1 in the MODEL statement activates this model.

Table II.5: Parameters for equations II-51 and II-52

Parameter	Value
E_{0N} (V/cm)	4.10^3
E_{0P} (V/cm)	4.10^3
γ_N	4
γ_P	1

II.4.4.2 Concentration-Dependent Low-Field Mobility

The commob parameter in ATLAS gives a doping dependent mobilities empirical data in the case of low-field for electrons and holes in silicon at a lattice temperature of 300K. These silicon mobility values are extracted from Figures II.2 and II.3.

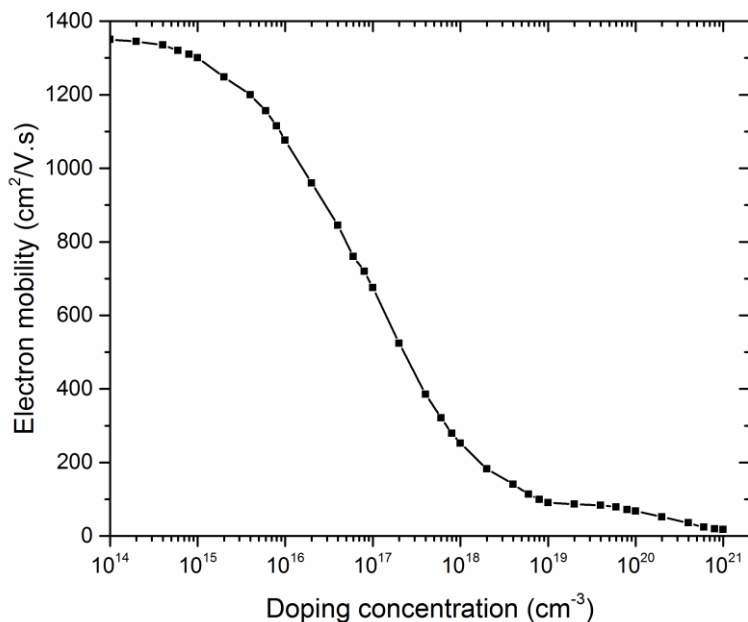


Figure II.2: Dependant concentration mobility of electrons in Si at 300K

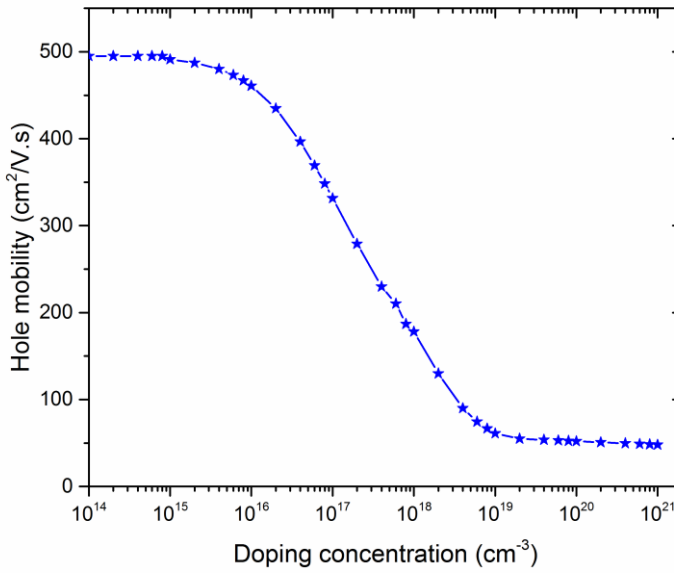


Figure II.3: Dependant concentration mobility of holes in Si at 300K

II.4.5 Statistics of Fermi-Dirac

Under equilibrium conditions $np = n_i^2$, where n is the concentration of electrons, p is the concentration of holes and n_i is the intrinsic carrier concentration which follows from the use of the equilibrium Fermi-Dirac distribution functions for electrons and holes:

$$f(E) = \frac{1}{1 + \exp\left(\frac{E - E_F}{k_B T_L}\right)} \quad (\text{II} - 53)$$

Where E_F is a spatially independent reference energy known as the Fermi level and k is Boltzmann's constant.

Under non equilibrium conditions, the representation of the distribution functions for electrons and holes is possible by introducing the quasi-Fermi levels, E_{Fn} and E_{Fp} , as follows:

$$f_n(E) = \frac{1}{1 + \exp\left(\frac{E - E_{Fn}}{k_B T_L}\right)} \quad (\text{II} - 54)$$

$$f_p(E) = 1 - f_n(E) \quad (\text{II} - 55)$$

$$= \frac{1}{1 + \exp\left(\frac{E - E_{Fp}}{k_B T_L}\right)} \quad (\text{II} - 56)$$

In the limit, $E - E_F \gg k_B T_L$, Equation (II-56) can be approximated as:

$$f(E) = \exp\left(\frac{E_F - E}{k_B T_L}\right) \quad (\text{II} - 57)$$

This equation is the base of Boltzmann statistics [29, 30]. Using Boltzmann statistics in place of Fermi-Dirac statistics simplifies subsequent calculations. Fermi-Dirac statistics are more necessary than Boltzmann statistics because they take into account some properties in very highly doped materials (degenerate).

II.4.6 Auger Recombination

Auger recombination is a three particle transition phenomena in which the carrier is being either emitted or captured [31].

II.4.6.1 Standard Auger Model

The modeling of Auger Recombination is as follows [32]:

$$R_{Auger} = C_n(pn^2 - nn_{ie}^2) + C_p(pn^2 - pn_{ie}^2) \quad (\text{II} - 58)$$

C_n and C_p are parameters given in Table II.6.

Table II.6: Parameters for equation II.58

Parameter	Default value
C_n (cm ⁶ /s)	2.8×10^{-31}
C_p (cm ⁶ /s)	9.9×10^{-32}

References

- [1] Vasileska, D., Goodnick, S.M.: Computational Electronics. Morgan & Claypool, Arizona (2006) pp. 04
- [2] Ravaioli, R.: Hierarchy of simulation approaches for hot carrier transport Bibliography 147 in deep submicron devices. *Semicond. Sci. Technol.* **13**, 1–10 (1998)
- [3] Apanovich, Y., Lyumkis, E., Polksy, B., Shur, A. and Blakey, P.: Steady state and transient analysis of submicron devices using energy balance and simplified hydrodynamic models. *IEEE Trans.* **13**, 702–7 (1994)
- [4] Atlas user's manual. <https://dynamic.silvaco.com/dynamicweb/silen/>. Accessed 30 January 2012
- [5] Maiti, C.K. and Armstrong, G.A.: Applications of Silicon–Germanium Heterostructure Devices. World Scientific Publishing Company, Singapore (2016) pp. 162
- [6] Maiti, C.K.: Computer Aided Design of Micro- and Nanoelectronic Devices. World Scientific Publishing Company, Singapore (2016) pp. 61
- [7] Stratton, R.: Diffusion of hot and cold electrons in semiconductor barriers. *Phys. Rev.* **126**, 2002–2014 (1962)
- [8] Stratton, R.: Semiconductor current-flow equations (diffusion and degeneracy). *IEEE Trans. Electron Devices* **19**, 1288–1292 (1972)
- [9] Lang, D.V.: Measurement of the band gap of $\text{Ge}_x\text{Si}_{1-x}/\text{Si}$ strained-layer heterostructures. *Appl. Phys. Lett.* **47**, 1333–1335 (1985)
- [10] Schaeffler, F.: High-mobility Si and Ge structures. *Semicond. Sci. Technol.* (1997). <https://doi.org/10.1088/0268-1242/12/12/001>
- [11] Slotboom, J.W.: The PN Product in Silicon. *Solid State Electronics* **20**, 279–283 (1977)
- [12] Slotboom, J.W. and de Graaf, H.C.: Measurement of bandgap narrowing in Si bipolar transistor. *Solid State Electron* **19**, 857–862 (1976)
- [13] Lanyon, H.P.D. and Tuft, R.A.: Bandgap narrowing in moderately to heavily doped silicon. *IEEE Trans. Electron Devices* **26**, 1014–1018 (1979)
- [14] Del Alamo, J.A. and Swanson, R.M.: Measurement of steady-state minority carrier transport parameters in heavily doped n-type silicon. *IEEE Trans. Electron Devices* **34**, 1580–1589 (1987)
- [15] Swirhun, S.E. Kwark, Y.H. and R.M. Swanson.: Measurement of electron lifetime, electron mobility and bandgap narrowing in heavily doped p-type silicon. In: IEEE IEDM Tech. Dig, pp. 24–27 (1986)

- [16] Klaassen, D.B.M. Slotboom, J.M. and De Graaff, H.C.: Unified apparent bandgap narrowing in n- and p-type silicon. *Solid State Electron* **35**, 125–129 (1992)
- [17] Slotboom, J.W. and de Graff, H.C.: Bandgap narrowing in silicon bipolar transistor. *IEEE Trans. Electron Devices* **24**, 1123–1125 (1977)
- [18] Shockley W., and Read W.T.: Statistics of the Recombination of Holes and Electrons. *Phys. Rev.* **87**, 835-842 (1952)
- [19] Hall, R.N.: Electron Hole Recombination in Germanium. *Phys. Rev.* **87**, 387 (1952)
- [20] Armstrong, G.A. and Maiti, C.K.: Technology Computer Aided Design for Si, SiGe and GaAs Integrated Circuits. The Institution of Engineering and Technology, London (2007) pp. 373
- [21] Roulston, D.J., Arora, N.D. and Chamberlain, S.G.: Modeling and Measurement of Minority-Carrier Lifetime versus Doping in Diffused Layers of n \pm p Silicon Diodes. *IEEE Trans. Electron Devices* **29**, 284-291 (1982)
- [22] Law, M.E., Solley, E., Liang, M., and Burk, D.E.: Self-Consistent Model of Minority-Carrier Lifetime, Diffusion Length, and Mobility. *IEEE Electron Device Letters* **12**, 401-403 (1991)
- [23] Fossum, J.G. and Lee, D.S.: A Physical Model for the Dependence of Carrier Lifetime on Doping Density in Nondegenerate Silicon. *Solid State Electronics* **25**, 741-747 (1982)
- [24] Arora, N.D., Hauser, J. R. and Roulston, D. J.: Electron and hole mobilities in silicon as a function of concentration and temperature. *IEEE Trans. Electron Devices* **29**, 292–295 (1982)
- [25] Klaassen, D.B.M.: A unified mobility model for device simulation—I. Model equations and concentration dependence. *Solid-State Electron* **35**, 953–959 (1992)
- [26] Klaassen, D. B. M.: A unified mobility model for device simulation—II. Temperature dependence of carrier mobility and lifetime. *Solid-State Electron* **35**, 961–967 (1992)
- [27] Caughey, D.M. and Thomas, R.E.: Carrier mobilities in silicon empirically related to doping and field. *Proc. IEEE* **55**, 2192–2193 (1967)
- [28] Barnes, J.J., Lomax, R.J. and Haddad, G.I.: Finite-element Simulation of GaAs MESFET's with Lateral Doping Profiles and Sub-micron Gates. *IEEE Trans. Electron Devices* **23**, 1042-1048 (1976)
- [29] Yu, Z., and Dutton, R.W.: SEDAN III-A Generalized Electronic Material Device Analysis Program. Stanford Electronics Laboratory Technical Report, Stanford University, (1985)
- [30] Joyce, W.B., and Dixon, R.W.: Analytic Approximation for the Fermi Energy of an ideal Fermi Gas. *Appl. Phys. Lett.* **31**, 354-356 (1977)

- [31] Selberherr, S.: Analysis and Simulation of Semiconductor Devices. Springer-Verlag/Wien, New York, (1984)
- [32] Dziewior J. and Schmid, W.: Auger Coefficient for Highly Doped and Highly Excited Silicon. *Appl. Phys. Lett.* **31**. 346-348 (1977)

Chapter III

SILVACO ATLAS

T-CAD DEVICE SIMULATOR

III.1 Introduction

In the herein chapter, ATLAS which is a device simulator from SILVACO TCAD and it is either two or three dimensional physically-based device simulator is used in the thesis work simulation. Atlas has the ability to predict the electrical behavior of different structures with specified semiconductor and it provides a preview of the internal physical mechanisms associated with the operation of the device operation.

The present chapter gives a full description of ATLAS focusing on its core functionality [1].

III.2 Simulation history

De Mari [2] reported the first 1D device simulator and Scharfetter *et al.* [3] for the 2D one. [4] gives a device simulation tools early history. 1D programs such as SUPREM and SEDAN from Stanford University [5] are considered as the beginning of simulation attempts, since this time, the fundamentals of device simulation were established. Programs such as MINIMOS [6], BAMBI [7], PISCES [8], BIPOLE [9] and HQUPETS [10] were able to solve the Poisson equation and the current continuity in 2D in the 1980s. By means of MINIMOS , Si, SiGe, GaAs and AlGaAs devices can be simulated. Heimeier [11] and Slotboom [12] gave 2D detailed transistor device simulations. A 2D BIPOLE device simulator predicts the terminal electrical characteristics of bipolar transistors. PISCES is also a 2D device simulator especially for MOS and bipolar [13]. From the early of the 1980s, some commercial simulators show the light such as: SILVACO, ISE-TCAD , TMA and AVENTi [14].

A set of physical models are provided by ATLAS from SILVACO such as drift-diffusion, hydrodynamic, energy balance transport models and lattice heating. Simulation of hot carrier injection, graded or abrupt heterojunctions, non-local impact ionization, band-to-band, stimulated emission and radiation, optoelectronic interactions are possible using Atlas.

III.3 ATLAS device simulator

In this thesis two 2D-simulations were created using the SILVACO ATLAS software. By the mean of this virtual software, the user can analyze the internal operation of semiconductor designs graphically without having to go inside growing, designing and testing processes of devices. The simulator is consists of interactive tools allowing the numerical simulation and electrical testing of devices.

The modules: ATLAS, DeckBuild, TonyPlot, DevEdit and LUMINOUS facilitate the simulation design. Relation between the previous modules is illustrated in Figure III.1 [1].

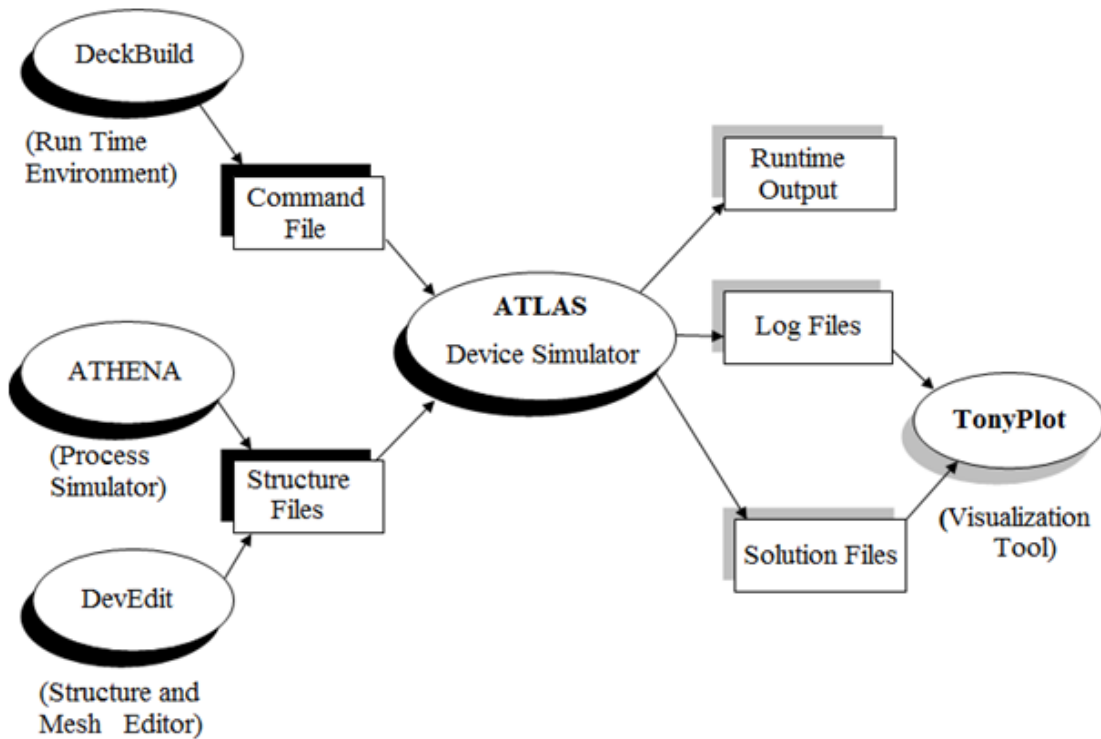


Figure III.1: Inputs and outputs in Atlas

III.3.1 Operation of ATLAS

Deckbuild is used in simulations in this thesis providing the information of device structure to ATLAS. This latter is able to run in several different modes that are with Deckbuild. Running ATLAS inside Deckbuild must use the syntax:

go atlas

This syntax will permit the start ATLAS simulator allowing it to input the code in Deckbuild with the stated conditions.

III.4 ATLAS Commands organization

The order of statements occurrence in ATLAS code is of great important. In Atlas there are five groups of statements and they must used in the correct order as presented in Figure III.2. The disorder of groups or statements leads to an error message causing incorrect operation or termination of the program. As example, the wrong order of the material parameters or models causes their elimination in the calculations. The statements order within the mesh definition, structural definition, and solution groups is important, too. The non respect of order may cause incorrect operation or program termination.

Group	Statements
1- Structure specification	- Mesh - Region - Electrode - Doping
2- Material model specification	- Material - Models - Contact - Interface
3- Numerical method selection	- Method
4- Solution specification	- Log - Solve - Load - Save
5- Results analysis	- Extract - Tonyplot

Figure III.2: command groups in Atlas

III.4.1 Structure Specification

Definition of the mesh, the region, the electrodes and the doping levels permit the specification of the structure.

III.4.1.1 Mesh

The input file starts by the structure initial mesh specification. The mesh command defines the lines location and spacing. x.mesh and y.mesh are used for two dimensional structures and in the case of three dimentional structures we add z.mesh.

X.MESH LOCATION=<VALUE> SPACING=<VALUE>

Y.MESH LOCATION=<VALUE> SPACING=<VALUE>

Example;

```
x.m  loc=-0.800  spacing=0.2
y.m  loc=-0.800  spacing=0.8
```

If accuracy is desired than small values in these commands yield finer meshing and increased accuracy at the expense of fast simulation. The use of large values at the beginning then create as fine mesh as possible towards the end is optimal to speed the simulation. In a 2D structure, Atlas automatically has a default value of one micrometer length in z direction. Minimizing the spacing at the center of the cell in the x direction is preferred. Mesh spacing always changes in every region at the y direction, and this depends on the region thickness.

In this thesis, meshing in the x direction is specified by the following commands:

```
x.m  
loc=0.00 spacing=0.1
```

```
x.m loc=0.060 spacing=0.02
```

```
x.m loc=0.085 spacing=0.01
```

```
x.m loc=0.105 spacing=0.01
```

```
x.m loc=0.125 spacing=0.01
```

```
y.m loc=-0.800 spacing=0.8
```

```
y.m loc=0.000 spacing=0.1
```

```
y.m loc=0.060 spacing=0.02
```

```
y.m loc=0.085 spacing=0.005
```

```
y.m loc=0.140 spacing=0.04
```

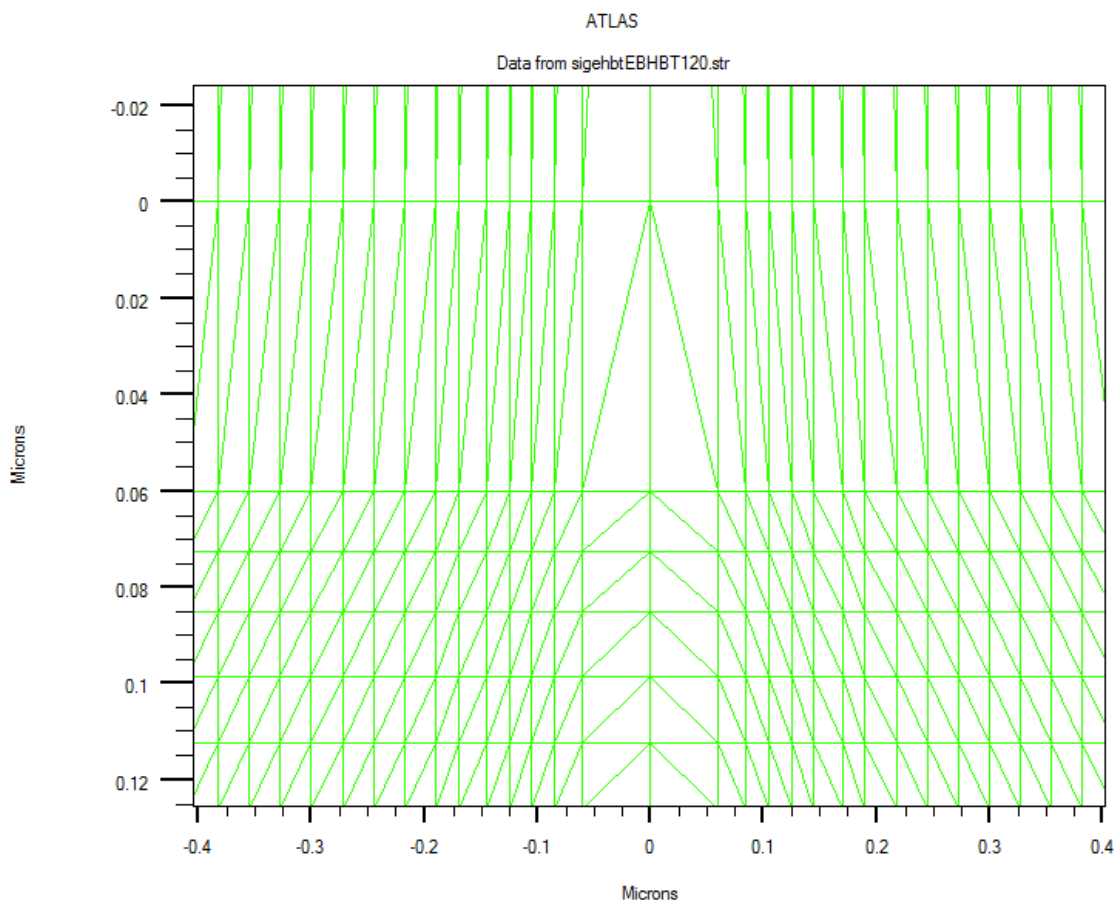


Figure III.3: ATLAS mesh creation

If one wants remove some lines than ELIMINATE statement is used.

Example:

```
ELIMINATE COLUMNS X.MIN=0.0 X.MAX=0.06 Y.MIN=0.0 Y.MAX=0.085
```

Automatic meshing gives a simpler method for device structures and meshes defining comparing to the manual method. Auto-meshing is particularly suited for epitaxial structures, especially device structures with many layers.

III.4.1.2 Region

To define a region In Atlas, we must divide the locations of the mesh into numbered areas. Region numbers must begin by 1 and are increased for each subsequent region statement. in ATLAS, you can define up to 200 different regions. Each region is associated with a specific material from the ATLAS library. Regions syntax is as follows:

REGION number=<integer> <material type> <position>.

Example:

region num=3 material=Si y.max=0.270 x.min=-0.190 x.max=0.190

The materials must be assigned to all mesh points in the structure. If not, ATLAS won't run successfully.

III.4.1.3 Electrodes

The definition of the regions and materials is followed by the contacts (electrodes) creation on the device. We must specify one contact at least in the code. In Atlas, up to fifty electrodes can be specified. The statement ELECTRODE is as follows:

ELECTRODE NAME = <electrode_name> <position parameters>.

Example:

elec name=emitter x.min=-0.105 x.max=0.105 y.max=0.0

X.MIN, X.MAX, Y.MIN, and Y.MAX parameters define the position and have microns units. The RIGHT, LEFT, TOP, and BOTTOM parameters in statement is also possible to define the location.

Example:

elec name=emitter top

III.4.1.4 Doping

Regions with a semiconductor material are allocated a type and level of doping concentration. The doping type is either n or p with uniform, linear, or Gaussian distribution. The concentration is in cm⁻³. The doping statement of doping is as follows.

DOPING <distribution type> <dopant_type> <position parameters>

Example:

doping uniform n.type conc=5.e20 region=4

Analytical doping profiles can have uniform, gaussian, or complementary error function forms.

doping gaussian concentration=1e18 characteristic=0.05 p.type \

x.left=0.0 x.right=1.0 peak=0.1

doping gauss p.type conc=8.e19 peak=0.1675 char=0.002 x.min=-0.170 x.max=0.170

This doping statement specifies a p-type Gaussian profile with a peak concentration of $8 \cdot 10^{19} \text{ cm}^{-3}$. This statement specifies that the peak doping is located along a line from $x = -0.170$ to $x = 0.170$ microns. Perpendicular to the peak line, the doping drops off according to a Gaussian distribution with a standard deviation of $(0.05/\sqrt{2}) \mu\text{m}$. At $x > -0.17$ or $x < 0.17$, the doping drops off laterally with a default standard deviation that is $(70/\sqrt{2})\%$ of characteristic as shown in Figure III-4.

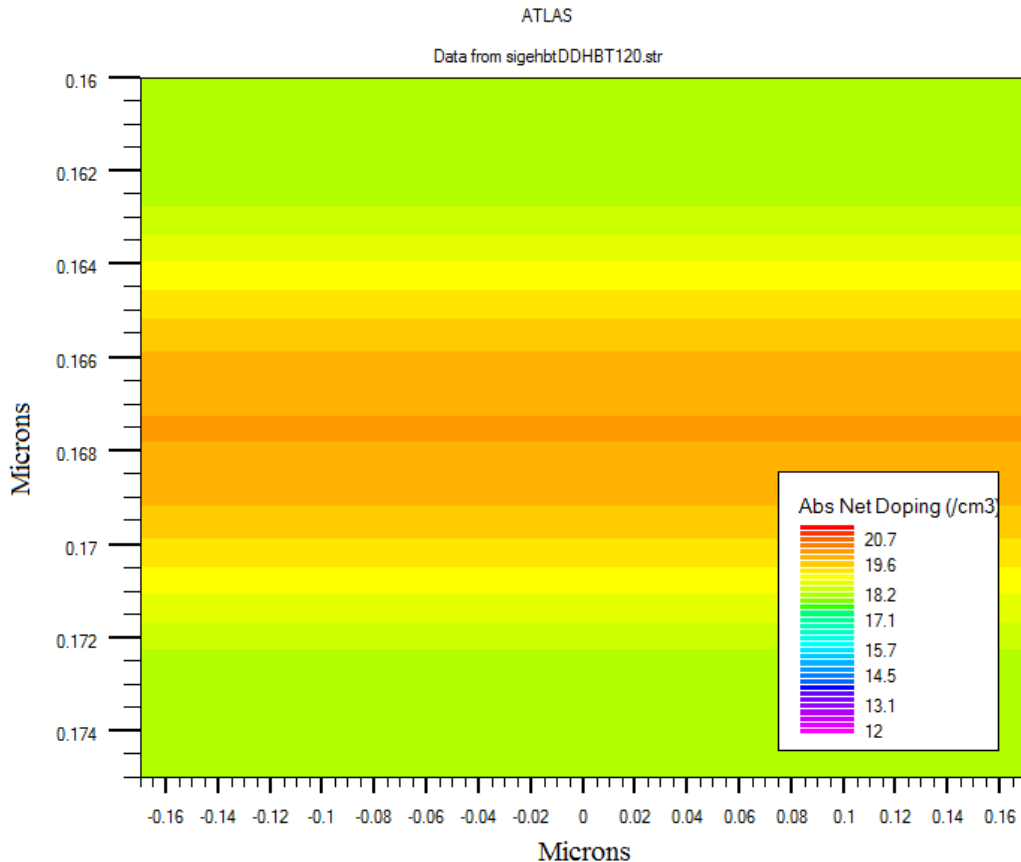


Figure III.4: Gaussian doping profile

III.4.2 Materials Model Specification

After defining the mesh, geometry, and doping profiles, the modification of electrodes characteristics, change the default material parameters, and choosing which physical models is possible using the CONTACT, MATERIAL, and MODELS statements respectively.

Defining customized equations for some models is also possible using SILVACO C-INTERPRETER (SCI),

III.4.2.1 Specifying Material Properties

The specification of the material properties is of high importance and the setting is as follows.

III.4.2.1.1 Semiconductor, Insulator, or Conductor

In Atlas, materials are classified into: semiconductors, insulators and conductors. Each class is specified with different set of parameters. For example, electron affinity, band gap, density of states and saturation velocities are included for semiconductors.

Atlas uses some default properties parameters for many materials during device simulation.

III.4.2.1.2 Setting Parameters

The specification of the own material parameters is possible in the MATERIAL statement.

These parameters are applied to a specified material or a specified region.

Example:

```
material material=SiGe taun0=1.e-8 taup0=1.e-8 F.CONMUN=mobility.lib \
F.CONMUP=mobility.lib
```

Sets the Shockley-Read-Hall recombination lifetimes and the electron and hole mobility in a SiGe region in the device.

III.4.2.2 Specifying Physical Models

To specify physical models the statements MODELS and IMPACT are used. Parameters for these models appear on many statements including: MODELS, IMPACT, MOBILITY, and MATERIAL.

There are five classes of physical models: mobility, recombination, carrier statistics, impact ionization, and tunneling

The previous models are specified on the MODELS statement except impact which is specified on the IMPACT statement.

Example:

```
model material=Si bgn consrh auger fldmob commob fermi print
In this statement, the band gap narrowing, the concentration dependent Shockley-Read-Hall recombination, the parallel field mobility, the concentration dependent mobility and Fermi Dirac statistics models should be used.
```

III.4.2.2.1 Using the C-Interpreter to Specify Models

The use of the C language interpreter permit the specification of several models and this is possible by means of ATLAS .lib file.

example:

```
material material=SiGe taun0=1.e-8 taup0=1.e-8 F.CONMUN=mobility.lib\
F.CONMUP=mobility.lib
```

F.CONMUN=mobility.lib contains the C-INTERPRETER function for the specification of the electron mobility model.

III.4.2.3 Contact Characteristics

Setting the contact characteristics is possible in Atlas.

III.4.2.3.1 Workfunction for Gates or Schottky Contacts

An electrode is by default ohmic in contact with semiconductor material. When a work function is mentioned then electrode is treated as a Schottky contact.

example:

```
CONTACT    NAME=anode    WORKFUNCTION=4.9
```

Sets the work function of the Schottky contact named anode to 4.9eV.

III.4.2.3.2 Shorting Two Contacts

ATLAS gives the possibility to tie two or more contact together. This is very useful such as in dual base bipolar transistors as in our work

Example:

```
contact name=base1      common=base      short
```

```
contact name=collector1  common=collector short
```

Here, base1 and base will be linked together also collector1 and collector will be linked together. The applied 0.1V on base will then appear on base1. ATLAS will calculate and store separate currents for both base1 and base. The SHORT parameter in the CONTACT statement above indicates that only a single base current will appear combining the currents from base and base1.

III.4.3 Numerical Methods

In Atlas, there are some numerical calculation methods.

III.4.3.1 Numerical Solution Techniques

Several numerical methods exist to calculate solutions of semiconductor device problems. In Silvaco Atlas, there are three types of solution techniques:

- a- decoupled (GUMMEL)
- b- fully coupled (NEWTON)
- c- BLOCK.

The GUMMEL method solves for each unknown and keeping the other variables constant, repeating the process until achieving stable solution.

The NEWTON method solves all the unknowns simultaneously .

The BLOCK method solves some equations fully coupled while others are de-coupled.

If the equations system is weakly coupled and has only linear convergence, the GUMMEL method is useful. If the system of equations is strongly coupled and has quadratic convergence then the NEWTON method is useful, however. NEWTON requires accurate initial guess to converge. The BLOCK method is preferable for faster simulations and it is much desired for energy balance simulations. Better initial guesses can be provided by

GUMMEL so starting a solution with a few GUMMEL iterations to achieve a better guess then switching to NEWTON to complete the solution.

The method is specified as follows:

METHOD GUMMEL BLOCK NEWTON

III.4.3.2 Basic Drift Diffusion Calculations

In the drift diffusion isothermal model, the three equations solution for potential, electron concentration, and hole concentration is required. The specification of GUMMEL or NEWTON alone gives simple Gummel or Newton solutions. The NEWTON method is the default one in all simulations.

Example:

METHOD GUMMEL NEWTON

The precedent statement means that the solution begins with some GUMMEL iterations before switching to NEWTON when convergence is not achieved which makes it robust way of obtaining solutions for any device despite consuming much time.

III.4.3.3 Energy Balance Calculations

In energy balance model, 5 coupled equations needs to be solved. GUMMEL specifies a decoupled solution and NEWTON specifies a fully coupled solution. BLOCK method performs a coupled solution of potential, carrier continuity equations followed by a coupled solution of carrier energy balance, and carrier continuity equations.

Switching from BLOCK to NEWTON is possible and this is done by specifying multiple solution methods in a single line.

Example:

METHOD BLOCK NEWTON

Here, calculation starts with BLOCK iterations. If convergence doesn't achieved then it switches to NEWTON. The previous method is the strongest approach for many energy balance applications.

III.4.4 Solution Specification

With ATLAS, the calculation of DC, AC small signal, and transient solutions is possible. By defining the voltages on each electrode in a device, ATLAS will calculate the current through each electrode. In addition to this, ATLAS will calculate carrier concentrations and electric fields quantities. During the simulation, the device always begins with zero bias on all electrodes. To obtain solutions, the bias is stepped from the initial equilibrium condition.

III.4.4.1 DC Solutions

The SOLVE statement is used in DC solutions.

Example:

```
solve Vbase=0.01
```

```
solve Vbase=0.05
```

The solution here begins with 0.01V then 0.05V on the base electrode. In the case of not specifying any voltage on any electrode, then ATLAS assumes the value from the last SOLVE statement.

III.4.4.1.1 Sweeping the Bias

The sweep of the bias is important and required in Atlas for most applications. Ramping the voltage of the base from 0.0V to 1.0V with 0.1V steps with a fixed 2.0V collector voltage, use we use the syntax:

```
SOLVE VCOLLECTOR=2.0
```

```
solve Vbase=0.1  Vstep=0.1  name=base  Vfinal=1.0
```

In name=base, the electrode name is quite sensitive. Make sure the initial voltage, the choose of the step is important so choosing 0.2V as a step for (Vbase=0.1V to Vfinale=1.1V) is not acceptable.

III.4.4.1.2 Initial Guess Importance

In Atlas, the good initial guess for the variables is of great importance to achieve convergence. For drift diffusion simulations, a poor initial guess leads to convergence problems of the solution.

In many cases, these methods are designed to overcome the problems associated with the initial guess. This is particularly important in simulations involving more than the three drift diffusion variables. Generally, coupled solutions require a good initial guess, whereas decoupled solutions can converge with a poor initial guess.

III.4.4.1.3 The Initial Solution

In the case of no previous solutions then from the doping profile the initial guess for potential and carrier concentrations is made. This explains the zero bias of the initial solution (thermal equilibrium). For that we use the statement:

```
SOLVE INIT
```

III.4.4.1.4 The First and Second Non-Zero Bias Solutions

The bias solutions of first and second non-zero are the most difficult in obtaining good convergence. If solutions are obtained, the projection algorithm for the initial guess is available and solutions should all have a good initial guess.

```
solve init
```

```
solve local Vcollector=2.0
```

III.4.4.1.5 The Trap Parameter

In ATLAS exists some methods to overcome the problem of a poor initial guess and other convergence difficulties. One way to overcome poor convergence is:

METHOD TRAP

If convergence problems exist then trap parameter reduces the bias step. Consider the example from the previous section:

```
solve init
```

```
solve local Vcollector=2.0
```

When convergence does not achieved, then the TRAP parameter cuts directly the bias step in half Vcollector = 1.0V and begins to solve. If convergence doesn't achieved again, then the bias step will be halved Vcollector = 0.5V. The parameter MAXTRAPS controls the maximum number of tries. When convergence is acedhiev, the bias steps are increased again to solve up to 2.0V. MAXTRAPS has a default value of 4 and it is not recommended to increase it, because the change of the syntax to use smaller bias steps is generally much faster.

III.4.4.2 Small-Signal AC Solutions

AC simulations are considered as a simple extension of the DC solution syntax. We summarize here two common types of AC simulation. AC simulations results are the conductance and capacitance between each pair of electrodes.

III.4.4.2.1 Ramped Frequency at a Single Bias

The ramp of frequency is required in some applications, as in determination of bipolar gain versus frequency. For this we use the syntax:

```
solve ac freq=10 fstep=10 mult.f nfstep=8 direct
```

The first solution starts with f=10Hz. A frequency ramp is used and FSTEP is in Hertz (fstep=10). The MULT.F parameter is used to specify that FSTEP is multiplication ramp (mult.f) for the frequency. This multiplies the frequency in successive steps from 10Hz to 1GHz.

Ramping both the bias and the frequency in Atlas is possible.

```
solve v2=0.025 v3=0.025 vstep=0.025 electr=23 nstep=2 ac freq=1e6 \
fstep=4 mult.f nfsteps=5
```

III.4.4.3 Run-Time Output

The Run-time output window is located at the bottom of the DeckBuild. It shows the errors appearing in the run-time output. The check of the run-time output of input files at the beginning of each new simulation is of great importance. This will help us to avoid any errors.

The visualization of the details of material parameters and constants and mobility models in the run-time output is gotten by specifying the parameter PRINT in the models statement. The use of the PRINT parameter gives us the opportunity of checking the parameters values and models used during the simulation as depicted in Figure III.5.

During SOLVE statements, the error numbers of each equation at each iteration are displayed.

Examples of the output:

```

CONSTANTS:
Boltzmann's constant = 1.38066e-023 J/K
Elementary charge = 1.60219e-019 C
Permitivity in vacuum = 8.85419e-014 F/cm
Temperature = 300 K
Thermal voltage = 0.025852 V

REGIONAL MATERIAL PARAMETERS:
Region : 1 2 3 4 5 6
Material : Si SiO2 Si SiO2 Si
Type : semicond. insulator semicond. semicond. insulator semicon

Average Composition Fraction
X-composition: 0 0 0 0 0 0
Y-composition: 0 0 0 0 0 0

Band Parameters
Epsilon : 11.8 3.9 11.8 11.8 3.9 11.8
Eg (eV) : 1.08 1.08 1.08 1.08 1.08 1.08
Chi (eV) : 4.17 4.17 4.17 4.17 4.17 4.17
Nc (per cc) : 2.8e+019 2.8e+019 2.8e+019 2.8e+019 2.8e+019 2.8e+019
Nv (per cc) : 1.04e+019 1.04e+019 1.04e+019 1.04e+019 1.04e+019 1.04e+019
ni (per cc) : 1.45e+010 1.45e+010 1.45e+010 1.45e+010 1.45e+010 1.45e+010

Bandgap narrowing parameters
bgn.e (eV) : 0.009 0.009 0.009 0.009 0.009 0.009
bgn.n (/cc) : 1e+017 1e+017 1e+017 1e+017 1e+017 1e+017
bgn.c : 0.5 0.5 0.5 0.5 0.5 0.5
ubgn.b : 3.1e+012 3.1e+012 3.1e+012 3.1e+012 3.1e+012 3.1e+012
ubgn.c : 3.9e-005 3.9e-005 3.9e-005 3.9e-005 3.9e-005 3.9e-005
bgn.shnk.me : 0.321 0.321 0.321 0.321 0.321 0.321
bgn.shnk.mh : 0.346 0.346 0.346 0.346 0.346 0.346
bgn.shnk.eps : 11.7 11.7 11.7 11.7 11.7 11.7
bgn.shnk.ge : 12 12 12 12 12 12
bgn.shnk.gh : 4 4 4 4 4 4

```

Figure III-5: Run-time output window for materials properties.

Figure III.5 shows us an example of the materials values (gap, density of states, affinity, temperature, etc...) applied in the simulation

prev	psi	n	p	psi	n	p
direct	x	x	x	rhs	rhs	rhs
i	j	m	-5.00*	-5.00*	-5.00*	-26.0*
<hr/>						
1	N	-9.43*	-9.20*	-10.6*	-27.8*	-15.41 -14.59
Electrode	Va (V)	Jn (A/um)	Jp (A/um)	Jc (A/um)	Jt (A/um)	
emitter	0.000e+000	-1.504e-017	-1.182e-020	-1.505e-017	-1.505e-017	
base	0.000e+000	1.145e-020	-3.413e-017	-3.412e-017	-3.412e-017	
collector	0.000e+000	-2.430e-017	-1.442e-020	-2.431e-017	-2.431e-017	
Total						-7.348e-017

Figure III.6: Run-time output window for calculation

The first three column headings: i, j, and m point out the iteration numbers of the solution and the solution method. i indicates the number of the outer loop iteration for decoupled solutions. J indicates the number of the inner loop.

The method is indicated by the letter m which can be:

G (gummel), N (newton), B (block), A (newton with autonr) or S (coupled Poisson-Schrodinger solution).

The results are being listed by ATLAS for each electrode in the case of achieving convergence. ATLAS produced also a big number of run-time output for complex simulations.

III.4.4.4 Log Files

When ATLAS calculates currents and voltages, they will be stored in log files. In DC simulations, these characteristics are calculated for each electrode. The time is also stored when the simulation is transient. In the case of alternating current simulations, the small signal frequency, the capacitances and the conductances can be saved.

Example:

```
log outf=sigehbtDDHBT1-120_1.log
```

The previous statement is called when we open a log file. DC and AC characteristics obtained in SOLVE statements which is located after the LOG statement are being stored and saved in the log file..

Log files contain only the terminal characteristics. They are typically viewed in TONYPLOT. Parameter extraction of data in log files can be done in DECKBUILD. Log files cannot be loaded into ATLAS to re-initialize the simulation.

III.5 Results analysis

Results in Atlas are allowed using extract and tonyplot parameters.

III.5.1 Parameter Extraction in DeckBuild

When solutions have been obtained using the parameter solve, we can display them graphically by means of TonyPlot. In addition, one can extract these parameters with the EXTRACT statement.

Example:

```
extract name="peak gain" max(i."collector"/ i."base")
```

The above example shows that the EXTRACT statement gives the current gain of an HBT. The informations of currents and voltages are previously saved in a log file named sigehtDDHBT120.log.

In the case of ac simulations, the Cut-off frequency and maximum oscillation frequency are of great importance. We define them as follows:

```
#  
# Extraction of parameters  
#  
extract init inf="sigehtDDHBT1-120_1.log"  
#  
# Maximum cutoff frequency  
extract name="Ft_max" max(g."collector""base"/(6.28*c."base""base"))  
#  
# Gummel plot  
extract name="max fT" max(g."collector""base"/(2*3.14*c."base""base"))  
#
```

III.5.2 Solution Files (tonyplot)

Quantities as the device structure, doping profiles, band parameters, electron and hole concentrations and electric fields can be plotted and this is done using TONYPLOT.

The syntax is:

```
save outf=sigehtDDHBT120.str  
tonyplot sigehtDDHBT120.str -set sigehtDDHBT120_doping.set
```

Here the structure of the device (HBT) is being plotted with the use of the parameter tonyplot. The concentration of electrons and holes, net doping, the bands diagrams and other quantities can also be visualized here, too.

```
output con.band val.band
```

this expression allowed the visualization of the conduction and valences bands.

```
log outf=sigehbtDDHBT120.log master
```

```
tonyplot sigehbtDDHBT120.log -set sigehbtDDHBT120.set
```

```
tonyplot sigehbtDDHBT120.log -set sigehbtDDHBT120_dccurrentgain.set
```

the first tonyplot permits the visualization of the gummel plot while the second one allows the visualization of the dc current gain.

References

- [1] Atlas user's manual. <https://dynamic.silvaco.com/dynamicweb/silen/>. Accessed 30 January 2012
- [2] de Mari, A.: An accurate numerical one-dimensional solution of the p-n junction under arbitrary transient conditions. *Solid State Electron.* **11**, 1021–1053 (1968)
- [3] Scharfetter, D.L., Gummel, H. K.: Large-signal analysis of a silicon read diode oscillator. *IEEE Trans. Electron Devices* **ED-16**, 64–77 (1969)
- [4] Krusius, J.P.: Process modelling for submicron complementary metal-oxidesemiconductor very large scale integrated circuits. *J. Vac. Sci. Technol.* **ED-24**, 905–911 (1986)
- [5] D'Avanzo, D.C., Vanzi, M., Dutton, R.W.: One-Dimensional Semiconductor Device Analysis (SEDAN). Report G-201-5, Stanford University (1979)
- [6] Selberherr, S., Schutz, A., Potzl, H.W.: MINIMOS – A Two-dimentional MOST transistor analyzer. *IEEE Trans. Electron Devices* **ED-27**, 1540–1550 (1980)
- [7] Franz, A.F., Franz, G.A.: BAMBI – A design model for power MOSFETs. *IEEE Trans. Comp. Aided Design* **CAD-4**, 177–189, (1985)
- [8] Jewell, R.E., Grabowski, W.B., Kump, M.R.: TCAD software from technology modeling associates. in Software Tools for Process, Device and Circuit Modeling, Dublin: Boole Press, 121–129 (1989)
- [9] BIPOLE3 User's Manual. <http://bipole3.com/mainframe.html>. (1993)
- [10] Armstrong, G.A. Denton, T.C.: HQUPETS – a two-dimensional simulator for heterojunction bipolar transistors. In Proc. IMA Conf. on Semiconductor Modeling, Loughborough, pp. 16–17 (1991)
- [11]. Heimeier, H.H.: A two-dimensional numerical analysis of a silicon N-P-N transistor. *IEEE Trans. Electron Devices* **ED-20**, 708–714 (1973)
- [12] Slotboom, J.W.: Computer-aided two-dimensional analysis of bipolar transistors. *IEEE Trans. Electron Devices* **ED-20**, 669–679 (1973)
- [13] PISCES. <http://www-tcad.stanford.edu/tcad/programs/pisces.html>. Stanford University (1994)
- [14] Armstrong, G.A., Maiti, C.K.: Technology Computer Aided Design for Si, SiGe and GaAs Integrated Circuits. the Institution of Engineering and Technology, London (2007), pp.8-10

Chapter IV

T-CAD SIMULATION RESULTS

AND DISCUSSIONS

IV.1 Introduction

In the work presented herein, the effects of the emitter and collector widths, the germanium trapezoidal profile shapes and base doping of a SiGe HBT on the DC current gain β_F , cutoff frequency f_T , and maximum oscillation frequency f_{MAX} were investigated with the drift-diffusion (DD), hydrodynamic (HD) and energy balance (EB) models using two-dimensional SILVACO technology computer-aided design (T-CAD) simulations. The SiGe HBT structure considered is based on state-of-the-art SiGe HBT technology [1–3].

IV.2 Effect of emitter and intrinsic collector widths on SiGe HBT performance

Graded introduction of germanium (Ge) into the base of a silicon (Si) bipolar junction transistor (BJT) to obtain a bandgap engineered complementary *npn* silicon–germanium (SiGe) heterojunction bipolar transistor (HBT) can have a significant effect on the tradeoffs involved in designing *npn* BJTs with matched performance and reliability [4–7]. Indeed, more attention is given to *npn* SiGe/Si heterojunction bipolar transistors (HBTs) in comparison with counterpart BJTs because of their superior frequency response characteristics. On the other hand, SiGe HBTs show great potential for use in high frequency and millimeter-wave applications [8]. The higher gain, speed, and frequency response of SiGe HBTs make these devices more competitive for use in technology areas where high-speed and high-frequency response are required [9]. The radiofrequency (RF) performance of SiGe HBTs has strongly improved over the last decade due to enhanced transit and maximum oscillation frequencies. This performance improvement was driven by shrinkage of lateral and vertical device dimensions in combination with innovative device configurations to decrease the parasitic effect of capacitances and resistances [10]. Recently, SiGe HBTs with maximum oscillation frequency f_{MAX} of 500GHz and transit frequency f_T of 300GHz were demonstrated [1–3].

It has been proved that description of the electrical performance of high-frequency SiGe HBTs using the drift-diffusion (DD) transport model is not accurate in the base and collector regions due to non-equilibrium carrier transport [11–13], in contrast to the energy balance (EB) transport model, which is based on the Boltzmann transport equation (BTE). The effects of the emitter and collector widths of a SiGe HBT on the DC current gain β_F , cutoff frequency f_T , and maximum oscillation frequency f_{MAX} were investigated with the drift-diffusion (DD) and energy balance (EB) models using two-dimensional SILVACO technology computer-aided design (T-CAD) simulations.

IV.2.1 Device structure

We carried out simulations to compare seven proposed SiGe HBT devices with different emitter and collector widths, as presented in Table IV.1. The device perimeter was the same in all seven cases except HBT6 and HBT7. The geometry of the studied SiGe HBTs is shown in Figure IV.1. The germanium (Ge) profile in the base and the vertical one-dimensional (1D) doping profile used in this work are shown in Figure IV.2. The Ge peak composition of the SiGe layer is taken equal to 0.28. A base Gaussian doping concentration of $8 \times 10^{19} \text{ cm}^{-3}$ is considered.

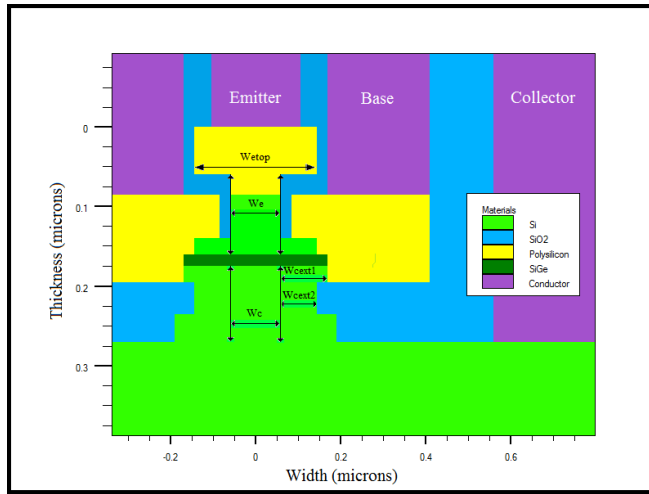


Figure IV.1: Simulated SiGe HBT structure. (The germanium profile in the base is trapezoidal. W_{etop} and W_e are the emitter cap and emitter widths, W_c and W_{cext} are the intrinsic and extrinsic collector widths)

Table IV.1: Emitter and collector widths for the seven studied HBTs

	HBT1	HBT2	HBT3	HBT4	HBT5	HBT6	HBT7
W_{etop} (nm)	290	290	290	290	290	250	250
W_e (nm)	120	100	80	100	80	100	80
W_c (nm)	120	100	80	120	120	120	210
W_{cext1} (nm)	$(340\text{nm}-W_c)/2$						
W_{cext2} (nm)	$(290\text{nm}-W_c)/2$						

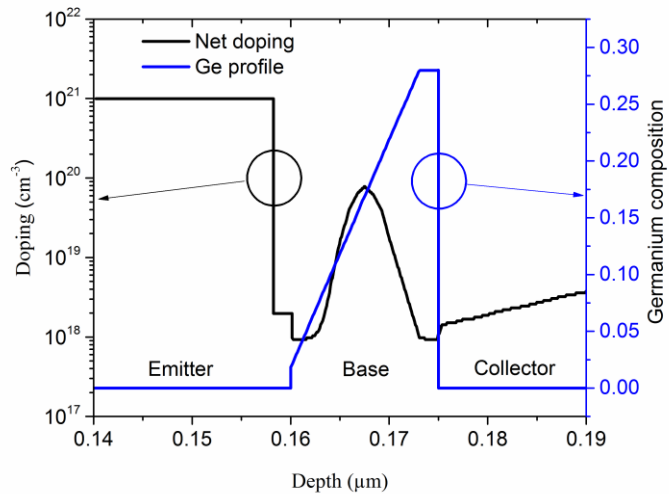


Figure IV-2: Germanium profile and doping used in the widths simulation [14]

The parameters used in this simulation such as the bandgap, density of states, effective lifetime, low-field mobility, and other parameters were taken from Refs. [15-16]. During all simulations, the physical models, doping, structural dimensions, and perimeter were kept unchanged, while the emitter and collector widths changed in each case as presented in Table IV.1.

IV.2.2 Effect of emitter and intrinsic collector widths on the current gain

The effects of the emitter and collector widths on the DC current gain β_F were studied based on drift-diffusion and energy balance Atlas SILVACO T-CAD simulations. Figure IV.3 shows the effect of germanium incorporation in the base and the doping on the conduction and valence bands. As shown in this figure, the trapezoidal germanium profile causes a reduction in the energy gap compared with silicon, which has the shape of a slope in the conduction band from the emitter to the collector side, accelerating electron transition and thereby enhancing the maximum oscillation frequency. The effect of the Gaussian *p*-type doping in the base is clearly visible in the band diagram, presenting a shift in the conduction band and especially the valence band.

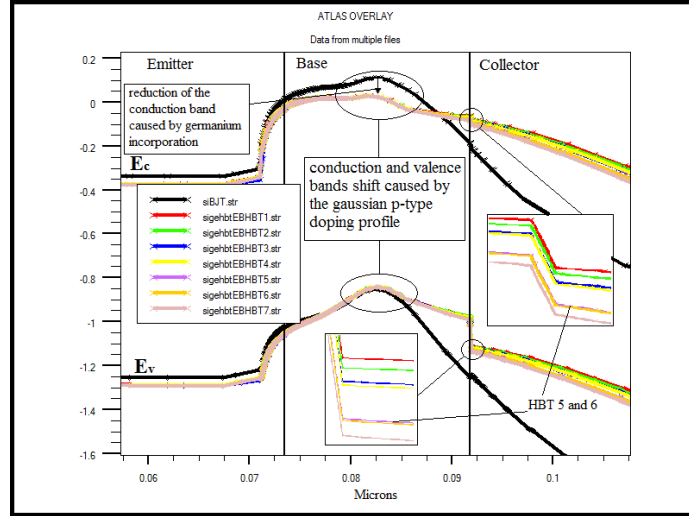


Figure IV.3: Band diagram for SiGe HBT1 to HBT7 in comparison with the Si BJT using the EB model; dimensions are arbitrary

The DC current gain obtained for devices HBT1, HBT3, HBT5, and HBT7 is shown in Figure IV.4. Based on the EB model, the HBT1, HBT3, HBT5, and HBT7 devices exhibited maximum current gain of 705, 685.4, 700.6, and 735.4, respectively, values close to the experimental data from Ref. [8]. It is clear that changing the emitter and collector widths W_e and W_c led to slight variation in the DC current gain. The lowest current gain of 685.4 was obtained for device HBT3 and the highest for device HBT7, presenting a difference in current gain of 50, equivalent to an increase of 7.3%. According to the simulations based on the DD model, there was no significant difference in the DC current gain as the emitter and collector widths were changed, as is clear from Figure IV.4, except for HBT7. The obtained current gain values are very small compared with the experimental values in Ref. [8]. The maximum DC current gain of 193.2 was obtained for HBT5 device, whereas the minimum DC current gain of 163.3 was obtained for device HBT7, a difference of 29.9, equivalent to a decrease of 15.47%.

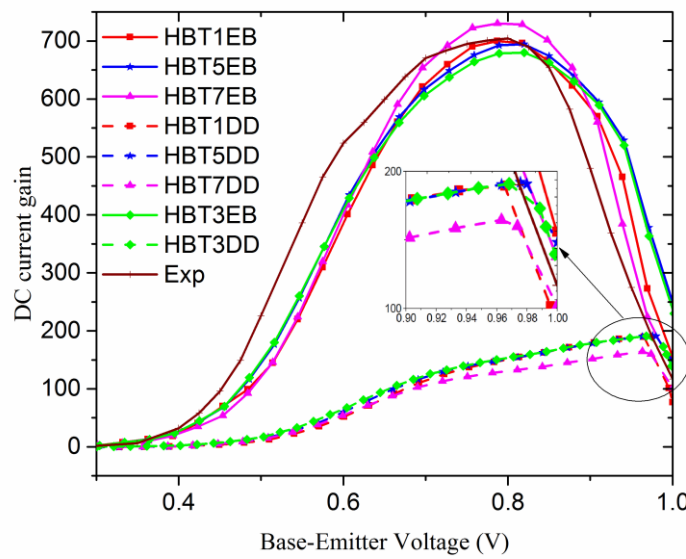


Figure IV.4: DC current gain versus base–emitter voltage for HBT1(squares), HBT3 (diamonds), HBT5 (stars), HBT7 (up triangles), and experimental results (pluses) [8] for the EB (solid lines) and DD model (dashed lines)

Table IV.2 recapitulates the current gain values obtained for the seven simulated devices using DD and EB simulations.

Table IV.2: The current gain values obtained for the seven simulated devices

	HBT1	HBT2	HBT3	HBT4	HBT5	HBT6	HBT7
EB	705	697.6	685.4	689.7	700.6	702.8	735.4
DD	189.7	189.6	191.5	190.6	193.2	193.2	163.3

IV.2.3 Effect of emitter and intrinsic collector widths on the gummel plots

Figure IV-5 shows an overlay of the Gummel plot for devices HBT1 and HBT5 obtained using the EB model. The Gummel plots for the two devices depict excellent characteristics for both collector and base currents.

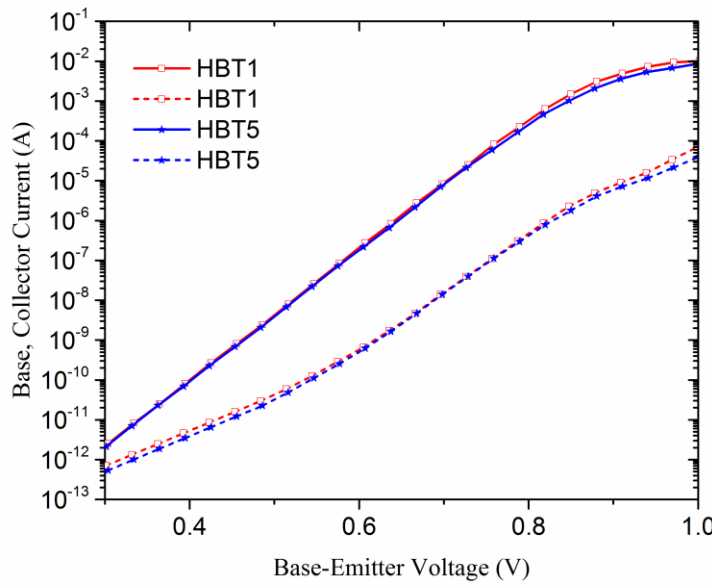


Figure IV.5: Gummel plots according to the EB simulation for HBT1 (open squares) and HBT5 (stars) for collector current (solid lines) and base current (dashed lines)

IV.2.4 Effect of emitter and intrinsic collector widths on the cut-off frequency and the maximum oscillation frequency

The effects of the emitter and collector widths on the cutoff frequency f_T , and maximum oscillation frequency f_{MAX} were studied based on drift-diffusion and energy balance with Atlas SILVACO T-CAD simulations. Based on the EB model, the f_T and f_{MAX} were obtained from the alternating-current (AC) current gain and the unilateral power gain U , respectively, as shown in Figure IV.6 and IV.7.

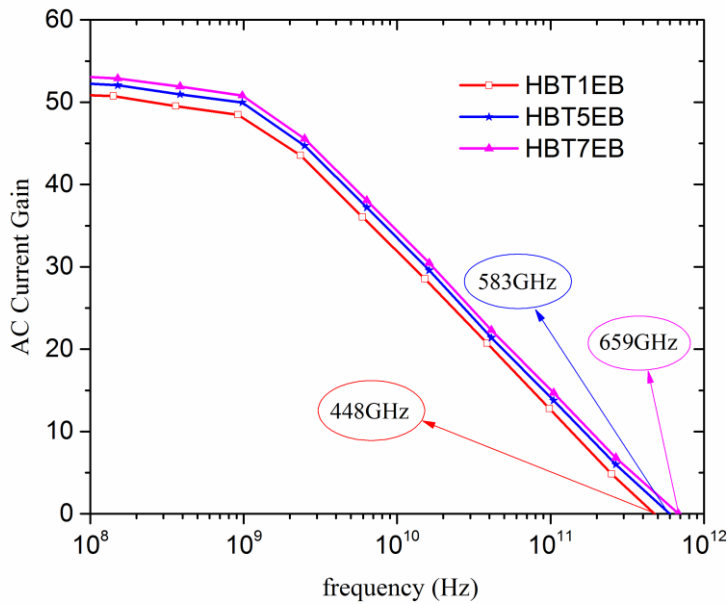


Figure IV.6: AC current gain versus frequency to determine the cutoff frequency f_T for device HBT1 (open squares), HBT5 (stars), and HBT7 (up triangles) using the EB model

Reduction of the emitter and collector widths (widths W_e and W_c) had a very limited effect on either the cutoff or maximum oscillation frequency. On the other hand, note that reduction of the emitter width (W_e) without reducing or increasing the collector width (W_c) led to an evident increase of both frequencies (f_T and f_{MAX}). Figure IV-6 shows the cutoff frequencies for devices HBT1, HBT5, and HBT7; an improvement of about 30% in f_T from HBT1 to HBT5 is noted. Reduction in the emitter width (W_e) with increase in the collector width (W_c) results in the highest cutoff frequency, with an increase of about 47.1% obtained from device HBT1 to HBT7. Meanwhile, the results for device HBT6 showed that reduction in both W_e and W_{etop} without changing the width W_c gives the best results, with an improvement of about 34% in f_T and 22.1% in f_{MAX} , mainly due to a decrease of the base resistance R_b and depletion capacitance C_{CB} . For the results obtained based on the DD model, the most noticeable improvement is for HBT2 device, for which f_T increases by about 19.49% and f_{MAX} by about 16.2% in comparison with HBT1.

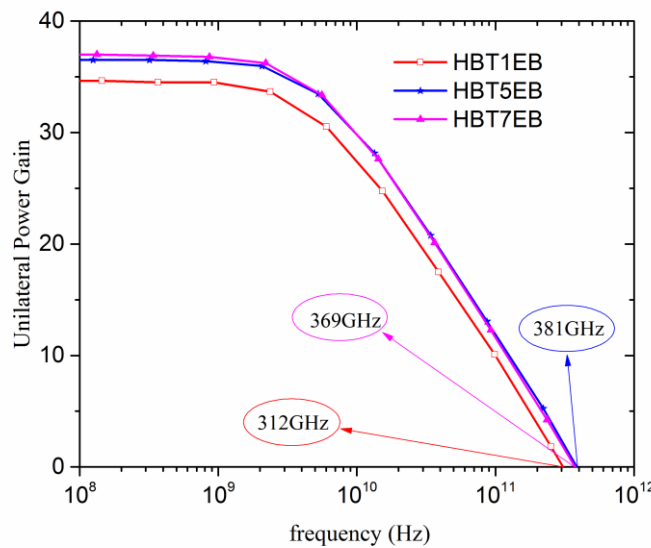


Figure IV.7: Unilateral power gain versus frequency to determine f_{MAX} for device HBT1 (open squares), HBT5 (stars), and HBT7 (up triangles)

Table IV.3 recapitulates the cut-off and maximum oscillation frequencies values obtained for the seven simulated devices using drift diffusion and energy balance transport models.

Table IV.3: Cut-off and maximum oscillation frequencies values obtained for the seven simulated devices

		HBT1	HBT2	HBT3	HBT4	HBT5	HBT6	HBT7
EB	f_T (GHz)	448	451	457	522	583	600	659
	f_{MAX} (GHz)	312	315	323	342	381	381	369
DD	f_T (GHz)	313	374	311	324	323	324	342
	f_{MAX} (GHz)	315	366	315	327	322	322	310

IV.2.5 Effect of emitter and intrinsic collector widths on the forward transit time

The forward transit time τ_F can be obtained from a graph of ($l/f_T = f(l/I_C)$), as illustrated in Figure IV-8. The intercept of the extrapolated straight line with the y-axis can be used to calculate τ_{F0} at low and medium current [18]. The τ_{F0} values simulated using the EB model are lower than (about 1.8 times) those obtained when using the DD model. Changing the emitter and collector widths (W_e and W_c) affected τ_{F0} ; these changes in transit time are caused by the variation of the time constant $R_c C_{jc}$ which is involved in τ_{F0} .

Table IV.4 summarizes the forward transit time τ_F obtained for the seven simulated devices using energy balance and drift diffusion simulation with Atlas from SILVACO T-CAD.

Table IV.4: Results of τ_{F0} for the seven devices from HBT1 to HBT7

		HBT1	HBT2	HBT3	HBT4	HBT5	HBT6	HBT7
EB	τ_{F0} (ps)	0.240	0.250	0.265	0.228	0.232	0.233	0.218
DD	τ_{F0} (ps)	0.425	0.440	0.463	0.415	0.420	0.422	0.408

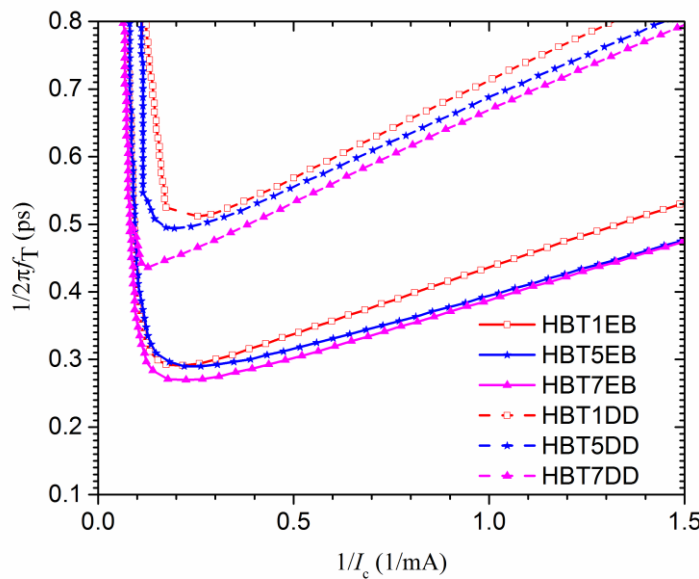


Figure IV.8: Transit time versus inverse of collector current obtained using DD model (dashed lines) and EB model (solid lines) for HBT1 (open squares), HBT5 (stars), and HBT7 (up triangles)

IV.3 Effect of germanium trapezoidal profile shapes on SiGe HBT performance

The effects of the shape of the trapezoidal profile on the direct current gain β_F , the cut-off frequency f_T and the maximum oscillation frequency f_{MAX} of SiGe hetero-junction bipolar transistor were studied. The energy balance, the hydrodynamic and the drift-diffusion transport models from SILVACO T-CAD were used to simulate these effects.

IV.3.1 Device structure

In this section, a comparison of three SiGe-HBTs is carried out using three different germanium trapezoidal profile shapes in the base: profile1 (HBT8), profile2 (HBT9) and profile3 (HBT10). Figure IV.1 shows the geometry of the studied SiGe-HBTs where W_c for the three devices is fixed to be 120nm, W_{etop} is taken to be 290nm and the germanium profiles are presented in Figure IV.9. In this study all the perimeters of the three hetero-junction transistors are kept the same, the unique change is reserved for germanium profile shape in the base. The parameters used in this simulation such as the bandgap, density of states, effective lifetime, low-field mobility, and other parameters are the same as in the previous section.

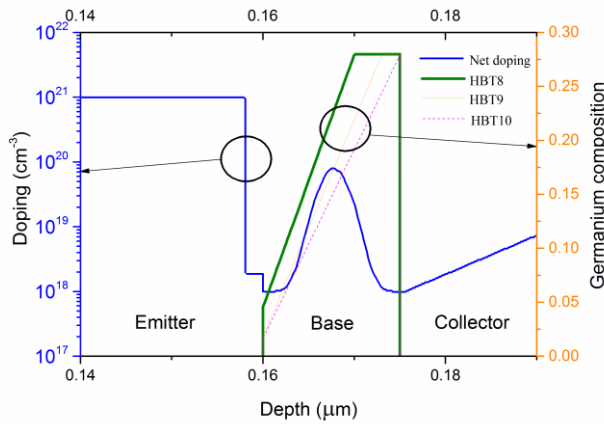


Figure IV.9: Germanium profiles and doping used in the trapezoidal shape simulation

IV.3.2 Effect of germanium trapezoidal profile shapes on the DC current gain

Effects of the trapezoidal profile shapes on the DC current gain β_F using drift diffusion, hydrodynamic and energy balance simulations of Atlas SILVACO T-CAD are studied. The DC current gains versus base-emitter voltage simulations of the three HBTs are shown in Figure IV.10. The devices HBT8, HBT9 and HBT10 have maximum current gains of 717,

705 and 680, respectively using energy balance transport model. The change of the germanium profile affects slightly the DC current gain; the gain decreases about 9% for DD and 5% for HD and EB transport models from HBT8 to HBT10. The change of the trapezoidal profile from profile1 to profile3 causes a small reduction in the collector current, base current and the current gain, too and this agrees with the theoretical equation which indicates that the gain enhancement varies exponentially with the germanium composition at the emitter end of the base, whereas it varies linearly with the grading. The values of β_F using EB simulation are higher than HD simulation (higher about 1.67 times) and much higher than DD ones (higher about 3.5 times). This difference in gain values between the models is due to non-local transport effects such as velocity overshoot, diffusion associated with carrier temperature gradients, and the dependence of impact ionization rates on carrier energy distributions which are neglected by the drift diffusion model. The current gain values of the three devices using the three transport models are exhibited in table IV.5.

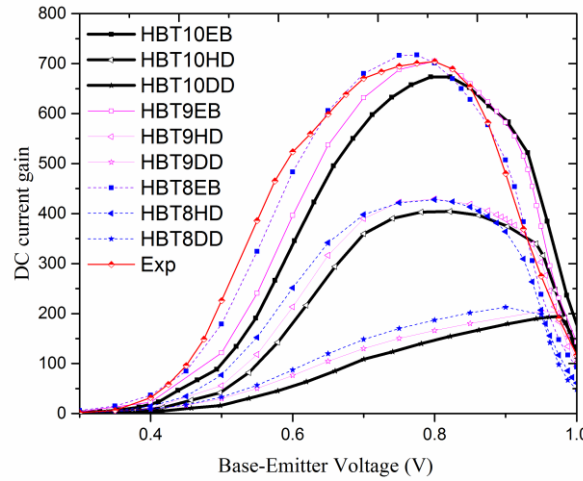


Figure IV.10: DC current gain versus base-emitter voltage. Half up diamond for experimental results from [8], dashed lines for HBT8, thin solid lines for HBT9 and thick solid lines for HBT10. Squares denote EB model, triangles denote HD model and stars denote DD model

Table IV.5: Results of β_F for the three devices HBT8, HBT9 and HBT10.

	DD			HD			EB		
	HBT8	HBT9	HBT10	HBT8	HBT9	HBT10	HBT8	HBT9	HBT10
β_F	212.7	204.8	194.8	427.8	429.4	407.2	717.1	705	680.7

IV.3.3 Effect of germanium profile shapes on the gummel plots

Figure IV.11 shows the overlay of the gummel plots of the three devices using EB simulation in comparison to experiment from reference [8]. HBT8 gummel plots exhibits excellent characteristics for both collector and base currents. The current gain and the gummel plots of HBT8 using EB model matched exactly the experimental measurement.

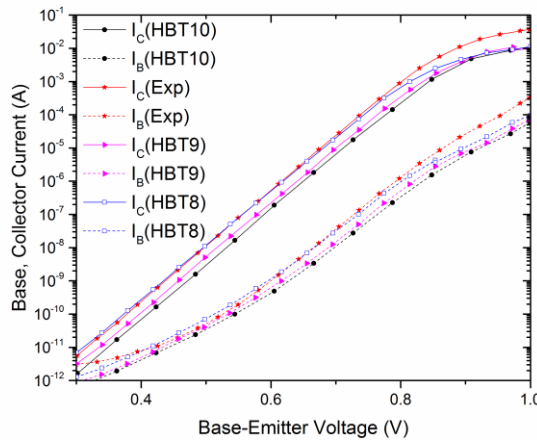


Figure IV.11: EB simulation gummel plots. Stars for experimental results [8], open squares for HBT8, triangles for HBT9 and circles for HBT10

IV.3.4 Effect of germanium profile shapes on the cut-off frequency and the maximum oscillation frequency

The cut-off frequency f_T was calculated according to $f_T = g_{cb}/(6.28 \times c_{bb})$ using drift diffusion, hydrodynamic and energy balance transport models with Atlas from SILVACO T-CAD and they are presented in Figure IV.12. The maximum oscillation frequency f_{MAX} was obtained from the unilateral power gain U , as shown in Figure IV.13.

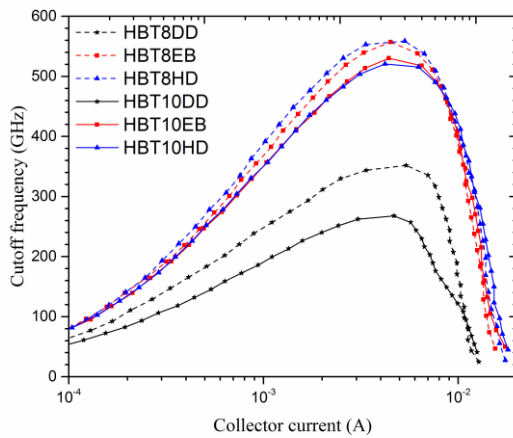


Figure IV.12: The cut-off frequency f_T for device HBT8 (dashed lines) and HBT10 (solid lines). Squares denote EB model, up triangles denote HD model and stars denote DD model

The cut-off frequency f_T decreases using HD and EB models from HBT8 to HBT10 and shows no significant change. The maximum oscillation frequencies extracted directly from unilateral power gain, increases from HBT8 to HBT10 using HD and EB transport models. This increase in figures of merit could be explained by that the reduction in the germanium concentration at the emitter side and the shifting of the germanium peak towards the base-collector junction has as consequence a decrease in the transit time leading to an enhancement in the frequencies, particularly in the maximum oscillation frequency f_{MAX} .

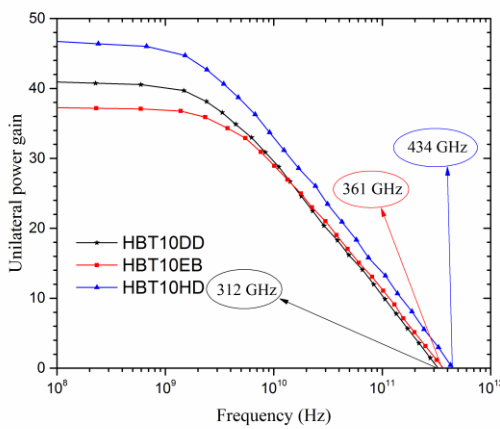


Figure IV.13: The unilateral power gain against frequency to determine f_{MAX} for device HBT10. Stars denote DD model, up triangles denote HD model and squares denote EB model. f_{MAX} is taken where gain tends to unity

Table IV.6 recapitulates and compares the cut-off and the maximum oscillation frequencies of the three devices under load using DD, HD and EB transport models.

Table IV.6: Results of f_T and f_{MAX} for the three devices HBT8, HBT9 and HBT10

	DD			HD			EB		
	HBT8	HBT9	HBT10	HBT8	HBT9	HBT10	HBT8	HBT9	HBT10
f_T (GHz)	354	311	268	566	538	527	559	547	531
f_{MAX} (GHz)	312	314	312	304	411	434	163	312	361

IV.4 Effect of base doping on SiGe HBT performance

The effects of the base doping on the direct current gain β_F , the cut-off frequency f_T and the maximum oscillation frequency f_{MAX} of SiGe hetero-junction bipolar transistor are studied. The energy balance transport model from SILVACO T-CAD was used to simulate these effects.

IV.4.1 Device structure

To study the effects of base doping, we consider three SiGe-HBTs with the same structure as of HBT1 presented in Figure IV.1 ($W_c=120\text{nm}$). The germanium profile of the three HBTs is the same as of HBT10 of figure IV-9. The HBTs base doping concentration is as follows: 8.10^{19} for HBT11, 9.10^{19} for HBT12 and 1.10^{20} for HBT13. The parameters used in this simulation such as the bandgap, density of states, effective lifetime, low-field mobility, and other parameters are the same as in the previous parties.

IV.4.2 Effect of base doping on current gain

The Figure IV.14 depicts the current gain versus the emitter-base voltage of the three HBTs previously considered. From the figure one can notice that the base doping affects considerably the current gain. Increasing the base doping (from HBT11 to HBT13), degrades the gain, and this is in agreement with equation (I-21). The values of current gain are 408, 358 and 326 for HBT11, HBT12 and HBT13, respectively. A reduction of about 20% from

HBT11 to HBT13 is noticed due to increase in base doping. Table IV.7 presents the values of the current gain of HBT11, HBT12 and HBT13.

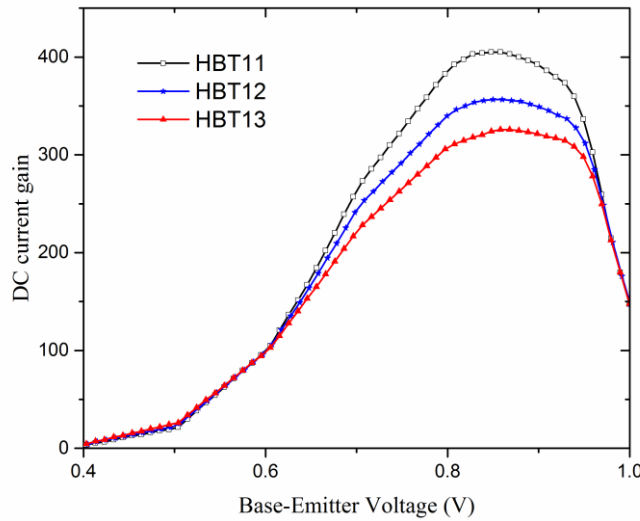


Figure IV.14: DC current gain versus base-emitter voltage. Squares for HBT11, stars for HBT12 and up triangles for HBT13 using EB model

IV.4.3 Effect of base doping on gummel plots

Figure IV.15 shows the overlay of the gummel plots of HBT11, HBT12 and HBT13 using EB simulation. The three devices gummel plots exhibit an excellent characteristics for both collector and base currents.

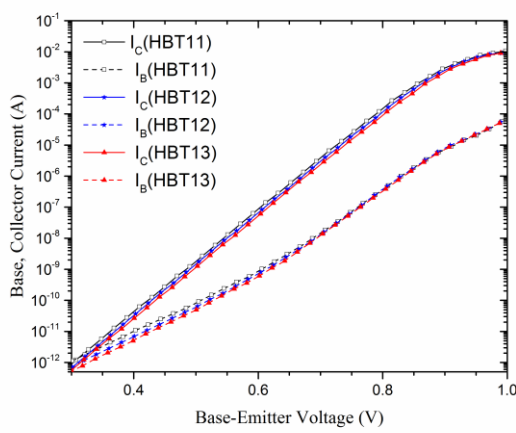


Figure IV.15: EB simulation gummel plots. Open squares for HBT11, stars for HBT12 and up triangles for HBT13

IV.4.4 Base doping effect on cut-off frequency and maximum oscillation frequencies

Increasing the base doping leads to a diminution in cut-off frequency as depicted in Figure IV.16. The cut-off frequencies of HBT11, HBT12 and HBT13 are: 517, 499 and 487, respectively. On the other side, the maximum oscillation frequencies of HBT11, HBT12 and HBT13 are: 500, 515 and 540 respectively. Figure IV.17 presents the unilateral power gain to extract the maximum oscillation frequency. We remark an enhancement in f_{MAX} which is mainly caused by the base doping increment. The f_{MAX} depends inversely on the base resistance R_b and the base-collector depletion capacitance C_{jc} as mentioned in equation (I-31). So high base doping causes a reduction in the base resistance and as a consequence an amelioration in f_{MAX} is obtained. Table IV.7 recapitulates the frequencies for the considered three devices.

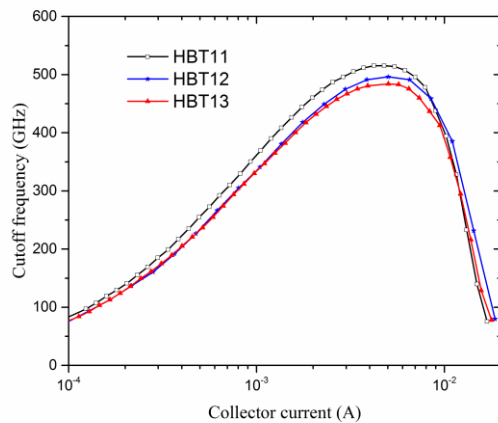


Figure IV.16: The cut-off frequency f_T for devices: HBT11 (open squares), HBT12 (stars) and HBT13 (up triangles) using EB simulation

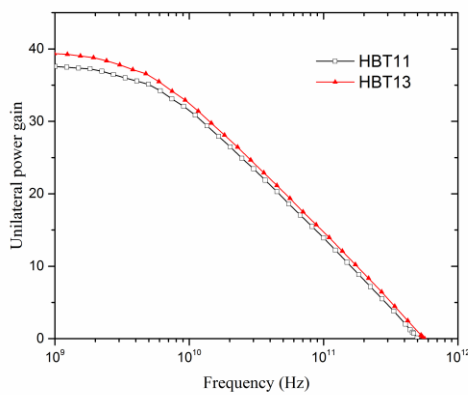


Figure IV.17: The unilateral power gain against frequency to determine f_{MAX} for devices: HBT11 (open squares) and HBT13 (up triangles) using EB simulation

IV.4.5 base doping effect on the forward transit time

Figure IV.18 shows the forward transit time τ_F which can be obtained from a graph of $l/f_T = f(l/I_C)$. τ_F is calculated from the intercept of the extrapolated straight line with the y-axis at low and medium current. The τ_{F0} values simulated using the EB model increase from HBT11 to HBT13. The base doping affected τ_{F0} and this is due to the variation of the base resistance which is involved in τ_{F0} .

Table IV.7: Results of β_F , f_T and f_{MAX} for the three devices HBT11, HBT12 and HBT13

	EB		
	HBT11	HBT12	HBT13
β_F	408	358	326
f_T (GHz)	517	499	487
f_{MAX} (GHz)	500	515	540
τ_{F0} (ps)	0.245	0.254	0.263

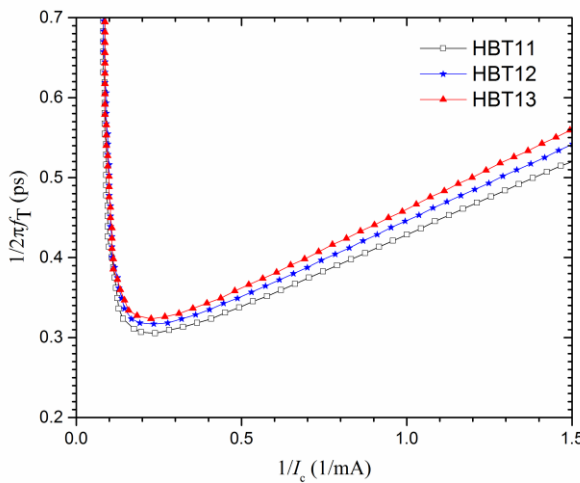


Figure IV.18: Transit time versus inverse of collector current obtained using EB model for HBT11 (open squares), HBT12 (stars) and HBT13 (up triangles)

IV.5 Conclusion

The effects of the emitter and collector widths, the base germanium profile shapes and the base doping on the DC current gain β_F , cutoff frequency f_T and maximum oscillation frequency f_{MAX} of SiGe HBTs were investigated using two dimensional (2D) energy balance (EB), hydrodynamic (HD) and drift-diffusion (DD) models. It was found that the DC current gain values obtained using the EB model were higher than the hydrodynamic ones and much higher than those obtained using the DD model. It is noticed that the base doping affects considerably the current gain whereas the change of emitter and collector widths and base doping profile shapes has little effect on the current gain.

Concerning the frequencies, it is remarked that the base doping and the base doping profile shape has a significant effect on the maximum oscillation frequency. Increasing the base doping and shifting the base germanium profile from the emitter side of the base towards the collector side of the base (triangular profile) enhance the maximum oscillation frequency.

References

- [1] Rücker, H., Heinemann, B., Fox, A.: Half-terahertz SiGe BiCMOS technology. In: IEEE 12th Topical Meeting on Silicon Monolithic Integrated Circuits in RF Systems, pp. 133–136 (2012)
- [2] Chevalier, P., Meister, T.F., Heinemann, B., Huylenbroeck, S.V., Liebl, W., Fox, A., Sibaja-Hernandezl, A., Chantre, A.: Towards THz SiGe HBTs. In: IEEE Bipolar/BiCMOS Circuits and Technology Meeting (BCTM), pp. 57–65 (2011)
- [3] Heinemann, B., Barth, R., Bolze, D., Drews, G., Fischer, G.G., Fox, A., Fursenko, O., Grabolla, T., Haak, U., Knoll, D., Kurps, R., Lisker, M., Marschmeyer, S., Rücker, H., Schmidt, D., Schmidt, J., Schubert, M.A., Tillack, B., Wipf, C., Wolansky, D., Yamamoto, Y.: SiGe HBT technology with f_T/f_{MAX} of 300/500 GHz and 2.0 ps CML gate delay. In: IEEE International Electron Devices Meeting (IEDM), pp. 688–691 (2010)
- [4] Chakraborty, P.S., Moen, K.A., Cressler, J.D.: An investigation on the optimization and scaling of complementary SiGe HBTs. *IEEE Trans. Electron Devices* **60**, 34–41 (2013)
- [5] Zhao, E., Sutton, A.K., Haugerud, B.M., Cressler, J.D., Marshall, P.W., Reed, R.A., El-Kareh, B., Balster, S., Yasuda, H.: The effects of radiation on 1/f noise in complementary (npn + pnp) SiGe HBTs. *IEEE Trans. Nucl. Sci.* **51**, 3243–3249 (2004)
- [6] Bellini, M., Jun, B., Sutton, A.K., Appaswamy, A.C., Cheng, P., Cressler, J.D., Marshall, P.W., Schrimpf, R.D., Fleetwood, D.M., El-Kareh, B., Balster, S., Steinmann, P., Yasuda, H.: The effects of proton and X-ray irradiation on the DC and AC performance of complementary (npn + pnp) SiGe HBTs on thick-film SOI. *IEEE Trans. Nucl. Sci.* **54**, 2245–2250 (2007)
- [7] Chakraborty, P.S., Appaswamy, A.C., Saha, P.K., Jha, N.K., Cressler, J.D., Yasuda, H., Eklund, B., Wise, R.: Mixed-mode stress degradation mechanisms in pnp SiGe HBTs. *IEEE International Reliability Physics Symposium (IRPS)*, pp. 83–88 (2009)
- [8] Zerounian, N., Aniel, F., Barbalat, B., Chevalier, P., Chantre, A.: 500 GHz cutoff frequency SiGe HBTs. *Electron. Lett.* **43**, 774–775 (2007)
- [9] Al-Sa'di, M., Fregonese, S., Maneux, C., Zimmer, T.: TCAD modeling of NPN-SiGe-HBT electrical performance improvement through extrinsic stress layer. In: IEEE 27th International Conference on Microelectronics Proceedings, pp. 387–390 (2010)
- [10] Rücker, H., Heinemann, B., Winkler, W., Barth, R., Borngräber, J., Drews, J., Fischer, G.G., Fox, A., Grabolla, T., Haak, U., Knoll, D., Korndörfer, F., Mai, A., Marschmeyer, S., Schley, P., Schmidt, D., Schmidt, J., Schubert, M.A., Schulz, K., Tillack, B., Wolansky, D.,

- Yamamoto, Y.: A 0.13 μm BiCMOS technology featuring f_T/f_{MAX} of 240/330 GHz and gate delays below 3 ps. *IEEE J. Solid State Circuits* **45**, 1678–1686 (2010)
- [11] Juan, M., Lopez-Gonzalez, J.M., Schröter, M.: Study of emitter width effects on β_F , f_T and f_{MAX} of 200 GHz SiGe HBTs by DD, HD and EB device simulation. *Semicond. Sci. Technol.* (2009). <https://doi.org/10.1088/0268-1242/24/11/115005>
- [12] Jungemann, C., Neinhuis, B., Meinerzhagen, B.: Comparative study of electron transit times evaluated by DD, HD, and MC device simulation for a SiGe HBT. *IEEE Trans. Electron Devices* **48**, 2216–2220 (2001)
- [13] Ieong, M.K., Tang, T.W.: Influence of hydrodynamic models in the prediction of sub-micrometer device char *Electron Devices* **44**, 2242–2251 (1997)
- [14] Shi, Y., Niu, G.: 2-D analysis of device parasitics for 800/1000 GHz f_T/f_{MAX} SiGe HBT. In: *Proceedings of the Bipolar/BiCMOS Circuits and Technology Meeting*, pp. 252–255 (2005)
- [15] Atlas user's manual. <https://dynamic.silvaco.com/dynamicweb/silen/>. Accessed 30 January 2012
- [16] Schaeffler, F.: High-mobility Si and Ge structures. *Semicond. Sci. Technol.* (1997). <https://doi.org/10.1088/0268-1242/12/12/001>
- [17] Vasileska, D., Goodnick, S.M.: *Computational Electronics*. Morgan & Claypool, Arizona (2006)
- [18] Rein, H.M.: Proper choice of the measuring frequency for determining f_T of bipolar transistors. *Solid-State Electron.* **26**, 75–82 (1983)

CONCLUSION

CONCLUSION

In this thesis, the effects of emitter and intrinsic collector widths, the base germanium trapezoidal profile shape and the base doping of SiGe heterojunction bipolar transistors operating at room temperature have been investigated. The drift diffusion, the hydrodynamic and the energy balance were used in the herein simulation. First, the physical operating principles of Si BJT and SiGe HBTs are reviewed. In the second part of the thesis, ATLAS device simulator from SILVACO T-CAD used in the present work is presented. The third chapter contains both general physical properties of Si and SiGe and physical models used in this work. In the final chapter, the results of the simulation are presented and discussed. The results of this study are of great importance; since they provide practical information which allows the developing an the understanding of physical changes of SiGe HBT caused by emitter and collector widths changes, germanium profile shape in the base and base doping.

The effects of the emitter and collector widths on the DC current gain β_F , cutoff frequency f_{MAX} , and maximum oscillation frequency f_{MAX} of SiGe HBTs were studied using two dimensional (2D) energy balance (EB) and drift-diffusion (DD) models. It was found that the DC current gain values obtained using the EB model were much higher than (more than 3 times) those obtained using the DD model. It was found that the change in the current gain values for the seven devices was not significant when using either the EB or DD model. The cutoff frequency obtained using the EB model was much (about 20–90%) higher than when using the DD model. The maximum oscillation frequency values obtained using the EB model were close to those obtained using the DD model, except for HBT5 and HBT6, for which the EB values were about 18% higher compared with those obtained using the DD model. Based on the EB simulation results, reduction of the emitter width (W_E) while keeping the collector width (W_C) unchanged causes an increase in the cutoff frequency (by up to 30% for HBT5 compared with HBT1) and the maximum oscillation frequency (by up to 22.11% for HBT5 in comparison with HBT1); these results show that one can improve both f_T and f_{MAX} with no remarkable change in β_F by making a tradeoff between the widths W_E and W_C without shrinking the transistor regions. On the other hand, it is important to note that reduction in both emitter (W_E) and collector (W_C) widths had no significant effect on f_T or f_{MAX} . However, it was found that increase of the collector width (W_C) while reducing the emitter width (W_E) gave an important improvement in f_T (by up to 47.1% from HBT1 to HBT7).

In the case of changing the germanium trapezoidal profile shape, it was found that the values of the current gain using EB model are higher than the HD ones (about 1.7 times) and much

higher than the DD ones (more than 3.5 times). For DD transport model, the f_T decreases from HBT8 to HBT10. The f_{MAX} remain the same for the three devices. The cut-off frequency increases remarkably using HD and EB models from HBT8 to HBT10. The f_{MAX} extracted from the unilateral power gain augments from HBT8 to HBT10 using HD and EB transport models which shows that the germanium profile shape is of great importance since it affects noticeably the maximum oscillation frequency.

The simulation results using energy balance model show that the base doping affects considerably both the current gain and the frequencies. The obtained current gain values decrease from HBT11 to HBT13 inversely with the base doping augmentation. The cut-off frequency decreases also from HBT11 to HBT13. We remark the amelioration of maximum oscillation frequency with the base doping increment and this is due to a reduction in the base resistance caused by base doping augmentation.

These results highlight remarkable differences between the three transport models. The causes leading to these differences must be determined and analyzed to keep using device simulation and develop promising compact models to understand the physical effects occurring in such devices.